Investigation of a Thermocapacitive Cycle by Aqueous Supercapacitors for Multifunctional Heat Pump and Energy Storage

Junyoung Kim[a,*], Bertan Özdoğru[b], Donal P. Finegan[b], Nelson James[b]

[a]*Kumoh National Institute of Technology, Gumi-si, Gyeongsangbuk-do, South Korea*

[b]*National Renewable Energy Laboratory, Denver West Parkway, Golden, CO, USA*

Abstract

Thermocapacitive cycles are promising thermal and energy storage cycles using supercapacitors, which can achieve thermal efficiencies over 50% of the Carnot limit. There is a lack of work investigating the use of thermocapacitive effects in practical heat pumps. This paper explores the design of thermocapacitive cells with higher temperature changes to be better suited for heat pumping applications. To evaluate the cell designs on temperature changes, pouch type cells are prototyped and modeled, and tested using a micro-calorimeter. A peak adiabatic temperature span of a LiCl aqueous cell is 2.7 °C. By arranging the cells in a cascade manner, the projected adiabatic temperature span can reach up to 30 °C with a heating density of 15 kW m^{-3} and an energy storage density of 1.65 kWh m^{-3}. Incorporating the energy storage capabilities into heating and cooling devices can be beneficial to building thermal management as energy storage becomes increasingly important for energy system integration.

Keywords: Thermocapacitive Cycle, Supercapacitor, Multifunctional, Heat Pump, Energy Storage, Calorimeter, Modeling

Nomenclature

*Correspondence

Email address: Junyoung.Kim@kumoh.ac.kr (Junyoung Kim)

Symbols

aC	Volumetric Capacitance	[F m^{-3}]
A	Area	[cm^2 or m^2]
c	Concentration	[mol m^{-3}]
C	Capacitance	[F]
c_p	Specific Heat Capacity	[J g^{-1} °C^{-1}]
C_p	Heat Capacity	[J °C^{-1}]
D	Diffusion Coefficient	[m^2 s^{-1}]
E	Electric Field	[V]
F	The Faraday Constant	[C mol^{-1}]
h	Convective Heat Transfer Coefficient	[W m^{-2} °C^{-1}]
I	Current	[A]
j	Current Density	[A m^{-2}]
J	Species Flux	[mol s^{-1} m^{-2}]
k	Thermal Conductivity	[W m^{-1} °C^{-1}]
L	Length	[m]
mc_p	Thermal Mass	[J °C^{-1}]
n or N	Number of Cycles or Number of Electrons	[-]
P	Pressure	[Pa]
q	Charge	[C]
$\dot{q}$	Area Normalized Heat Generation Rate	[W m^{-2}]
$\dot{q_v}$	Volumetric Heating Density	[kW m^{-3}]
Q	Electric Charge	[C]
Q_{tot}	Total Heat Delivered	[J]
$\dot{Q}$	Heat Generation Rate	[W]
$\overline{\dot{Q}}$	Average Heat Generation Rate	[W]
R	Resistance	[Ω]
R	The Universal Gas Constant	[J mol^{-1} °C^{-1}]
dS	Differential Entropy	[J °C^{-1}]
S	Entropy or Source	[J °C^{-1} or mol s^{-2} m^{-2}]
t	Time	[s]
T	Temperature	[°C]
u	Mobility	[s mol kg^{-1}]
U	Overall Heat Transfer Coefficient	[W m^{-2} °C^{-1}]
V	Voltage or Volume	[V or cm^3]
W	Work	[J]

y	Mass Fraction	[-]
z	Charge	[-]
Acronyms		
Bi	Biot Number	[-]
CMC	Carboxymethyl Cellouse	
COP	Coefficient of Performance	[-]
DSC	Differential Scanning Calorimetry	
DI	Distilled Water	
DL	Diffusion Layer	
ED	Energy Storage Density	[kWh m^{-3}]
EDL	Electric Double Layer	
EDLC	Electric Double Layer Capacitor	
HVAC&R	Heating, Ventilation, Air-Conditioning, and Refrigeration	
IHL	Inner Helmholtz Layer	
Nano-CT	X-Ray Nano Computed Tomography	
MAE	Mean Absolute Error	
OHL	Outer Helmholtz Layer	
SA:V	Surface Area to Volume Ratio	[m^{-1}]
TCC	Thermocapacitive Cycle	
TCHP	Thermocapacitive Heat Pump	
TEG	Thermoelectric Generator	
VC	Vapor Compression	
Greek Symbols		
α	Thermopower	[mV $°C^{-1}$]
Δ	Difference	[units vary]
ϵ	Porosity or Electrical Permittivity	[-]
σ	Electrical Conductivity	[S m^{-1}]
τ	Tortuosity Factor	[-]
ϕ	Potential	[V]
Subscripts & Superscripts		
amb	Ambient	
avg	Average	
c	Cooling or Cold or Charging	
case	Pouch Cell Case	
cd	Charge and Discharge	
cell	Cell	
chg	Charge	

cycle	Cycle
dischg	Discharge
eff	Effective
e	Electron
elec	Electrode
electrolyte	Electrolyte
even	Even Index Cells
f	final
h	Heating
H	High
i	Species i or initial
ion	Ion
irr	Irreversible
l	Liquid
L	Low
m	Migration
max	Maximum
odd	Odd Index Cells
out	Output
rev	Reversible
s	Solid
sep	Separator
span	Temperature Span
th	Thermal
tot	Total
T	Total
volume	Volume
+	Positive Electrode
−	Negative Electrode
∞	Surrounding

1. Introduction

The buildings' sector accounts for more than 40% of the U.S. primary energy usage, and nearly half of building energy usage is related to space cooling and heating, water heating, and refrigeration [1]. The global need for air conditioning and heat pumping systems is expected to significantly increase in the next decade, driven by population growth, economic advancement, and environmental factors [2, 3]. Vapor compression (VC) cycles are the most widely used systems to provide cooling and heating. Recently, significant research efforts have been made to transition to VC systems using natural refrigerants. These systems generally require trade-offs in capacity, efficiency, system pressure, and flammability [4]. Therefore, several research groups are actively pursuing the development of new types of heat pumps beyond VCs that can help reduce energy consumption and improve energy utilization in the building sector [5].

Non-VC technologies have started to gain more attention as alternatives to conventional heating and cooling systems due to their potential for superior performance and the ability to use alternative refrigerants [6]. The next generation of high-performance thermal systems will utilize novel materials to achieve superior levels of performance [7, 8]. Maximizing the functionality of system hardware presents new opportunities for advancing thermal systems in addition to ongoing efficiency advancements. Hybridization strategies present an unique opportunity to increase the utility of thermal devices while simultaneously incorporating high-efficiency processes [9, 10].

Thermocapacitive cycles (TCCs) can enable a new generation of building equipment, such as multifunctional heat pumps and storage devices. TCCs are based on electric double layer capacitors (EDLCs), which are inherently electrical energy storage devices [11]. Using porous electrodes, these devices electrostatically bind ions to their surface, which absorbs and releases heat [12]. Similar to caloric heat pumping devices [13], this phenomenon could be used to develop an efficient heat pump through heating the cells in a cascade manner and transferring heat to a circulating fluid.

Leveraging thermocapacitive effects, Lin et al. [11] designed a thermocapacitive heat engine for harvesting low-grade heat, which showed the maximum power output of 31.9 W and 51.2% of the Carnot limit at the temperature lift of 90 °C. Kundu and Fisher [14] experimentally assessed a thermocapacitive power generation and electrical energy storage, which showed a Seebeck

coefficient of -1.2 mV °C^{-1} and an area-specific capacitance of 13 F cm^{-2}. Buckingham et al. [15] evaluated the performance of a thermocapacitive power generation and energy storage device using superabsorbent hydrogel materials. The maximum power density of the system was 95 mW m^{-2} and capacitance density was 220 F cm^{-2} at the temperature lift of 20 °C. Zhao et al. [16] showed that hybridized thermocapacitive power cycles with dye-senitized solar cells have potentials to achieve the power density and thermal efficiency of 149 W m^{-2} and 14.9%, respectively. Recently, Lao et al. [17] experimentally discussed the impacts of thermal voltage rise and self-discharge on the fundamental limitations of thermocapacitive heat engines, and the practical operational conditions toward high-efficiency low-grade heat harvesting.

Despite the significant promise of TCC technologies, a lack of work has been done on using thermocapacitive effects for practical heat pumping applications. In regards to liquid-state thermocells [18, 19], science and engineering research institutes are mainly focused on thermocapacitive cell design for waste heat recovery. Although James et al. [20] developed a proof-of-concept prototype for thermocapacitive cooling, the analysis was based on commercial supercapacitors that are not optimized for heat pumping and their main focus was a system-level analysis. This was due to the lack of information on the thermocapacitive cell design as well as the electrode/electrolyte materials and porous structures of the commercial cells. Because capacitive devices are the key elements for TCCs to achieve higher temperature lifts, there is a critical need for investigating the influence of electrode/electrolyte combination on thermocapacitive effects and the impacts of cell designs on the system performance. Challenges that must be addressed include developing designs with: (1) sufficient temperature lifts, (2) efficient heat recuperation, and (3) ensuring material compatibility for long life.

Moreover, limited research has been done on incorporating energy storage capabilities into cooling and heating devices. Supercapacitors used in the TCCs have the potential to provide electrical energy storage densities as high as 60-88 kWh m^{-3} [21, 22]. Their mechanism for storing energy is rapid adsorption/desorption of electrolyte ions on the surface of carbon electrodes, which is more suitable for faster demand responses than battery-type devices [17]. Moreover, the TCC technologies can be a cost-competitive heat pump and energy storage solution since supercapacitors can be manufactured with relatively abundant electrode materials like activated carbon and aqueous

electrolytes and can avoid supply chain issues associated with critical materials usage [23]. Incorporating electrochemical energy storage capabilities into heat pumping applications could be useful for advancing building thermal systems by enabling grid interactive buildings for next generation energy system integration [24].

This paper explores the design of thermocapacitive cells with higher adiabatic temperature changes to be better suited for heat pumping applications. To evaluate the material choices and cell designs on the temperature changes, pouch type cells were prototyped and modeled. The thermocapacitive cells were manufactured with relatively abundant materials like activated carbon and aqueous electrolytes. A micro-calorimeter was used to quantify the heat generation rates and temperature changes of the prototyped cells. A multiphysics cell model was developed that incorporates thermal, electrochemical, and fluid effects to aid in cell designs. A thermocapacitive heat pump (TCHP) model was developed to explore potential system configurations to find ones that have larger temperature spans and minimized heat losses. Lastly, the findings of this work were compared with the performance of the state-of-the-art electrochemical and caloric heat pumping as well as thermal energy storage technologies. Future research and development opportunities were discussed to advance the technology readiness level of the TCHP for practical heat pumping.

2. System Description

Figure 1(A) describes the working principle of thermocapacitive heating and cooling based on EDLCs. Slow charging of a thermocapacitive cell electrostatically binds ions to their electrode surface, forming electric double layer (EDL). The EDL consists of inner Helmholtz layer (IHL), outer Helmholtz layer (OHL), and diffusion layer (DL). The IHL is a compact layer that accumulates the counterions near the porous electrodes, whereas the OHL and DL are the extension of the IHL that contains movable ions affected by electrostatic forces and diffusion [25].

The formation of those layers decreases ionic configuration entropy (S_{ion}) due to the reduced disorder of ions within the bulk electrolyte. This is counterbalanced by increasing the electrolyte entropy and cell temperature (i.e., reversible heating) based on the second law of thermodynamics, i.e., $dS = 0$. Slow discharging of the cell desorbs ions from the electrode sur-

face, decreasing the electrolyte entropy and cell temperature (i.e., reversible cooling) [12].

Figure 1(B) shows a voltage-charge (V-q) diagram of an ideal TCHP cycle consisting of four processes: adiabatic charging, heat rejection at constant charge, adiabatic discharging, and heat absorption at constant charge. The cell is adiabatically charged from state ① to state ②, increasing temperature and voltage. From state ② to state ③, the cell rejects heat to hot thermal reservoir at constant charge, which decreases the cell voltage due to the voltage-temperature relationships within the cell [28]. From state ③ to state ④, the cell is isentropically discharged, decreasing temperature and voltage. From state ④ to state ①, the cell absorbs heat from a cold thermal reservoir at constant charge, increasing the cell voltage.

Figure 1(C) shows an operation principle for one cycle of a TCHP with multiple cells. The cells transfer the heat to the forward x-direction by alternating the charged and discharged cells as described below.

- Adiabatic charging (① → ②): Even index cells charge (cell heat up) while odd index cells discharge (cell cool down).
- Heat rejection at q_{H} (② → ③): Even index cells contact adjacent odd cells with higher index to transfer heat in x-direction.
- Adiabatic discharging (③ → ④): Even index cells discharge (cell cool down) while odd index cells charging (cell heat up).
- Heat absorption at q_{L} (④ → ①): Even index cells contact adjacent odd cells with lower index to transfer heat in x-direction.

The system is based on fully solid-state regeneration using dynamic thermal contacts, such as thermal diodes [26] or switches [27]. Those actuators could selectively choose cells for heat exchange on either side. Hot and cold side heat exchangers (i.e., heater and cooler) are placed at the opposite ends of each secondary loop to harness the warmer fluid leaving the stack for heating and the cooler fluid leaving the stack for cooling. Two liquid pumps are used to drive fluid circulation. Electrical charge can be stored in the cells when the heat pump is turned off and used it as needed.

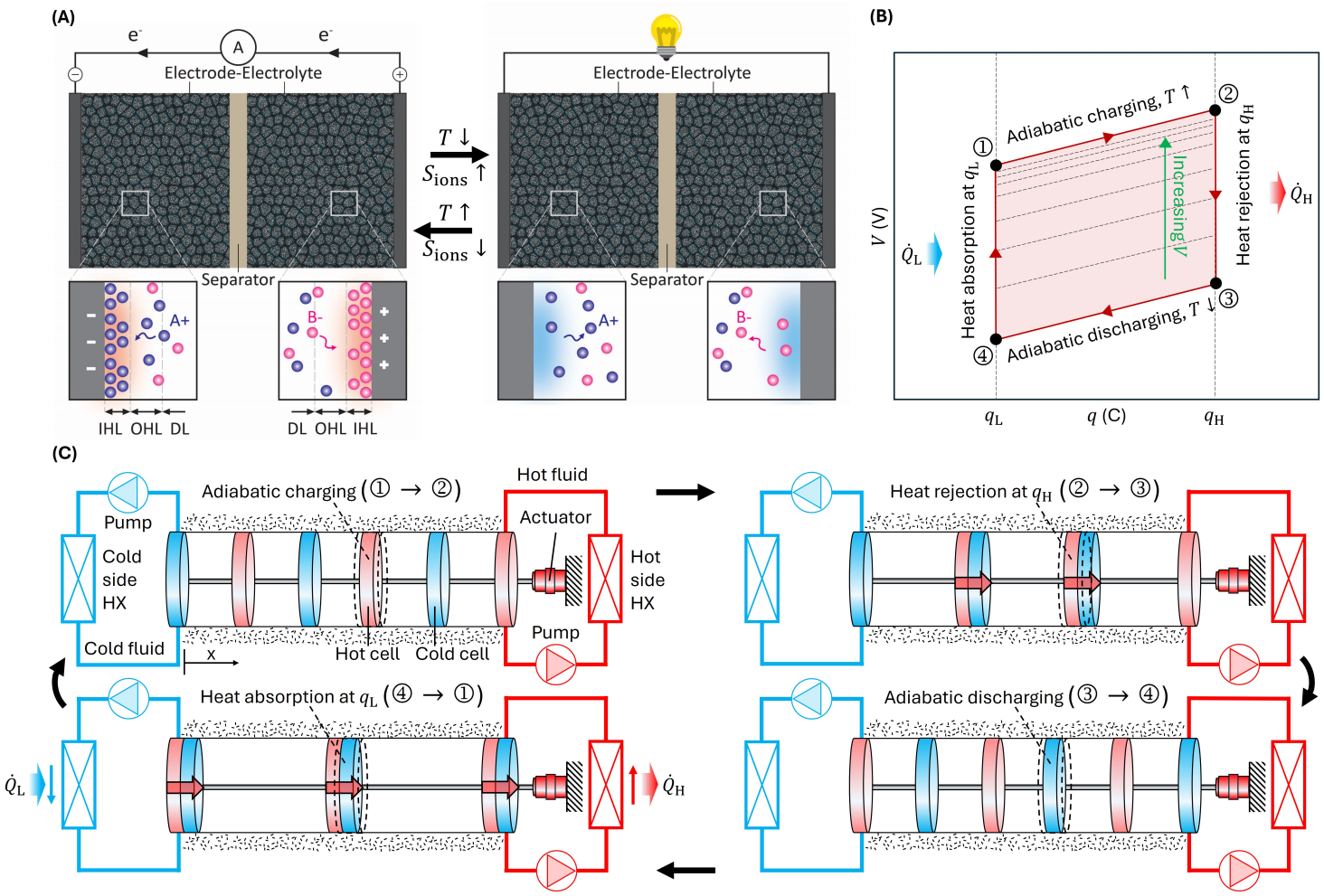

Figure 1: Thermocapacitive mechanism for multifunctional heat pumping and electrical energy storage. (A) Slow charging of a thermocapacitive cell forms EDL consisting of IHL, OHL, and DL. The formation of EDL electrostatically binds ions to the electrode surface, which releases heat and increases electrolyte temperature (reversible heating). Whereas slow discharging of the cell desorbs ions from the electrode surface, which absorbs heat and decreases electrolyte temperature (reversible cooling). (B) A voltage-charge (V-q) diagram of a TCHP cycle. (C) An operation principle for one cycle of a TCHP with multiple cells. The cells transfer the heat to the forward x-direction by alternating the charged and discharged cells. The system is based on fully solid-state regeneration using dynamic thermal contacts, such as thermal diodes [26] or switches [27]. Those actuators could selectively choose cells for heat exchange on either side. Electrical charge can be stored in the cells when the heat pump is turned off and used it as needed.

3. Methodology

3.1. Thermodynamics of thermocapacitive heating and cooling

For closed simple systems with given internal restraints, stable equilibrium states can be characterized completely by two independently variable properties in addition to the masses of the particular chemical species initially charged [29].

This means that a fundamental thermodynamic relation for the specific or molar entropy is $S = S(T, P, N)$, where N is chemical species. For thermocapacitive cells, a fundamental thermodynamic relation of the form $S = S(T, P, Q)$ is chosen because N is equal to electric charge (Q). This is because thermocapacitive effects induce an entropy change through the changes in the number of electric charges (species) over the electrodes.

A total differential of dS can be expressed as Eq. (1).

$$dS = \left(\frac{\partial S}{\partial T}\right)_{\mathrm{P,Q}} dT + \left(\frac{\partial S}{\partial P}\right)_{\mathrm{T,Q}} dP + \left(\frac{\partial S}{\partial Q}\right)_{\mathrm{T,P}} dQ \tag{1}$$

where S is entropy, T is temperature, and P is pressure. The heat capacity of electrolyte at constant pressure and electric charge is defined as $C_{\mathrm{P,Q}} = T\left(\frac{\partial S}{\partial T}\right)_{\mathrm{P,Q}}$, resulting in Eq. (2).

$$\left(\frac{\partial S}{\partial T}\right)_{\mathrm{P,Q}} = \frac{C_{\mathrm{P,Q}}}{T} \tag{2}$$

For isentropic ($dS = 0$) and isobaric ($dP = 0$) processes, Eq. (1) becomes Eq. (3).

$$dT = -\frac{T}{C_{\mathrm{P,Q}}}\left(\frac{\partial S}{\partial Q}\right)_{\mathrm{T,P}} dQ \tag{3}$$

Employing a Maxwell relation [11], the adiabatic temperature change of electrolyte during charging/discharging follows a thermodynamic identity as described in Eq. (4):

$$dT = \frac{T}{mc_{\mathrm{p}}} \left(\frac{\partial V}{\partial T} \right)_{\mathrm{Q}} dQ \tag{4}$$

where m (in g) is electrolyte mass, c_{p} (in J g^{-1} °C^{-1}) is specific heat capacity of electrolyte for a given pressure, and V (in V) is the cell voltage. For aqueous electrolyte at moderate ion concentration, the change in heat capacity of ion ($c_{\mathrm{p,q}}$) is insensitive to the change in the number of ions (q), resulting in $c_{\mathrm{p,q}} \approx c_{\mathrm{p}}$ at isobaric conditions [12].

Thermopower (α_{rev}, in mV °C^{-1}) refers to an effective Seebeck coefficient for electrochemical cells, which describes a material's ability to generate an electric current from heat or vice versa [18]. α_{rev} has been defined as $\left(\frac{\partial V}{\partial T}\right)_{\mathrm{Q}}$ [28]. Employing the definition of α_{rev}, the time derivative of Eq. (4) becomes Eq. (5).

$$mc_{\mathrm{p}} \frac{dT}{dt} = \underbrace{\alpha_{\mathrm{rev}} IT}_{\dot{Q}_{\mathrm{rev}}} \tag{5}$$

The right-hand side of Eq. (5) is equivalent to reversible heat generation rates ($\dot{Q}_{\mathrm{rev}}$) [30]. For isothermal ($dT = 0$) and isobaric ($dP = 0$) processes, the change in entropy is calculated by Eq. (6).

$$\Delta S = \alpha_{\mathrm{rev}} \Delta Q \tag{6}$$

where ΔS (in J °C^{-1}) is the change in entropy and ΔQ is the change in electric charge.

3.2. Micro-calorimeter and calorimetry

Calorimetric experiments were performed to quantify the heat generation rates and temperature changes of the prototyped cells during galvanostatic cycling.

Figure 2(A) shows a photo of a micro-calorimeter which was capable of sensing and quantifying heat transfer rate as low as 1 mW [31]. Figure 2(B) and (C) illustrate a CAD drawing of the calorimeter showing a cross-sectional view and exploded view of the stackup cell. The calorimeter was based on

Bi_2Te_3 thermoelectric generators (TEGs) (1261G-7L31-04CL; Custom Thermoelectric) as heat flux sensors. A 2×2 configuration of four TEGs (9 cm^2 of each, totaling 36 cm^2) was used, where each TEG's heat source faced the cell and heat sink faced outwards. The cells were sandwiched between two custom-designed Cu heat spreaders (busbars). Thermal grease (TC-5600, Dow Corning) and calibrated springs (pressure of 137.9 kPa) were used to minimize the contact resistance between the cell and each heat spreader.

Figure 2(D) depicts a schematic of calorimetry and equivalent thermal circuit. The entire unit was sealed in an aluminium heat sink that was submerged in an isothermal temperature bath at 30 °C (7008 high precision bath, Fluke) with 50:50 by volume ethylene glycol:deionized water. The electrochemical cycling was performed using a multichannel cycler (Arbin Instrument) connected to the cells inside of the calorimeter. An Agilent 34970A data acquisition (34970A, Keysight) was used to measure the currents, voltages, and heat generation rates of the cells, with the time interval of nearly 1.5 s.

Prior to cell testing, the calorimeter was calibrated using a thin polyimide resistive heater (Polyimide, Kapton) placed between the heat spreaders. A linear relationship between TEG voltage outputs and heat generation rates was obtained by providing a series of heating powers (0-32 mW) from an electric heater and measuring the TEG voltage outputs at each electrode. It was assumed that the electric heater has a thermal efficiency of 100%. A total heat generation rate was assumed to be equal to the sum of heat transfer rate at each TEG (see Supplemental Note S1 for details on the calorimeter calibration).

The time constant of the calorimter refers to the characteristic time it takes to reach thermal equilibrium of 63.2% after heat transfer is introduced. This metric represents how quickly the temperature inside the calorimeter can be stabilized [32]. For the prescribed galvanostatic current densities of 8.3-16.6 A m^{-2}, the time required for a charging and discharging cycle (6-12 min) is longer than the time constants of the calorimeter (2-7 min). This means the calorimetric experiments are reasonable to assess the transient heat and temperature profiles of thermocapacitive cells (see Supplemental Note S1 for details on the time constant of the calorimeter).

The calculation of uncertainty propagation was performed using a linear

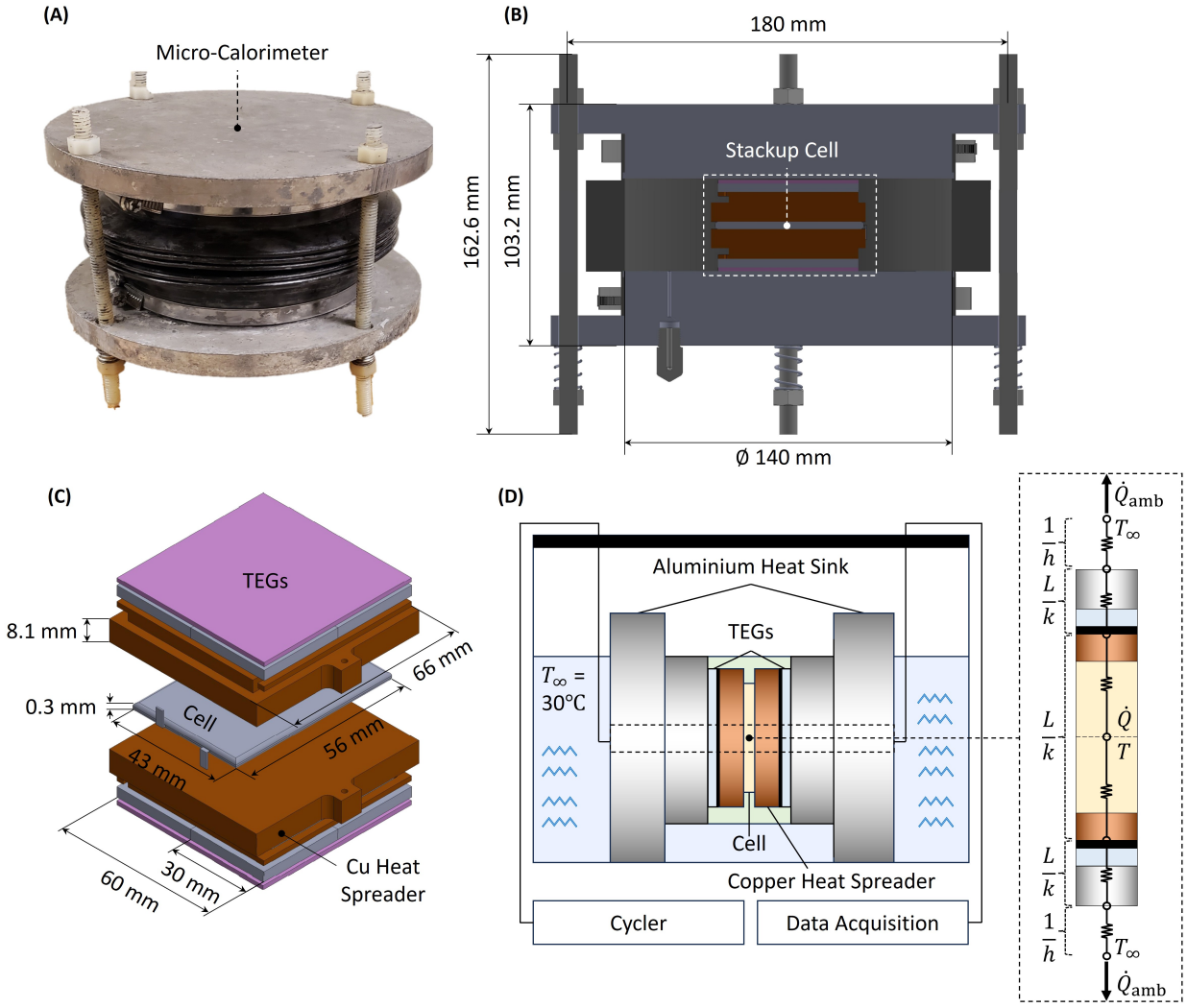

Figure 2: Micro-calorimeter [31]. (A) A photo of the micro-calorimeter. (B) A CAD drawing of the micro-calorimeter showing a cross-sectional view and (C) exploded view of the stackup cell. (D) A schematic of calorimetry and an equivalent thermal circuit.

error propagation theory [33]. For example, the total uncertainty of a given calculated value M is calculated by Equation 1.

$$\varepsilon_M = \sqrt{\sum_{\mathrm{j}} \left(\frac{\partial M}{\partial x_{\mathrm{j}}} \varepsilon_{\mathrm{j}} \right)^2} \qquad \text{(Equation 1)}$$

where ε_M is the total uncertainty of a given calculated value M and the x_{j} and ε_{j} are the uncertainties of each measured value and each absolute uncertainty, respectively. The partial derivatives were analytically derived. After input of sensor measurement uncertainties, the total uncertainties of the calculated variables ($\dot{Q}$, T) were calculated. The uncertainty of the total heat generation rates ($\varepsilon_{\dot{Q}}$) was 0.4 mW (see Supplemental Note S1). The uncertainties of the cell temperature (ε_T) at U = 1, 5, and 100 W m^{-2} °C^{-1} are 0.2, 0.03, and 0.002 °C, respectively.

The methodologies for analyzing the heat generation rates of supercapacitors from calorimetric experiments [34, 35, 36] were adopted in this study. The heat generation rate ($\dot{Q}$) is decomposed into irreversible ($\dot{Q}_{\mathrm{irr}}$) and reversible ($\dot{Q}_{\mathrm{rev}}$) heat generation rates, as given by Eq. (7).

$$\dot{Q} = \dot{Q}_{\mathrm{irr}} + \dot{Q}_{\mathrm{rev}} \tag{7}$$

$\dot{Q}_{\mathrm{irr}}$ is given by Eq. (8).

$$\dot{Q}_{\mathrm{irr}} = \frac{1}{t_{\mathrm{cd}}} \oint_{\mathrm{cycle}} \dot{Q} dt \tag{8}$$

where t_{cd} is charging and discharging time. $\dot{Q}_{\mathrm{rev}}$ is calculated by Eq. (19).

$$\dot{Q}_{\mathrm{rev}} = \dot{Q} - \dot{Q}_{\mathrm{irr}} \tag{9}$$

As charging time-averaged $\dot{Q}_{\mathrm{rev}}$ is given by Eq. (10).

$$\overline{\dot{Q}}_{\mathrm{rev}} = \frac{1}{t_{\mathrm{c}}} \int_{(n-1)t_{\mathrm{cd}}}^{(n-1)t_{\mathrm{cd}}+t_{\mathrm{c}}} \dot{Q}_{\mathrm{rev}} dt \tag{10}$$

where n is cycle number, t is time, and subscript c and cd correspond to charging, and charging and discharging, respectively.

Since the calorimeter was designed to quantify the heat fluxes from cells, an equivalent thermal circuit was used to predict the temperature of the cells, as shown in Figure 2(D). Conservation of energy was applied to a control mass (i.e., cell), which becomes Eq. (11).

$$T = T_\infty + \frac{\dot{Q}}{UA} \tag{11}$$

where U is overall heat transfer coefficient, A is surface area of a cell, and T_∞ is surrounding temperature. The U was calculated by $1/U = 1/h + L_1/k_1 + L_2/k_2$, with h is convective heat transfer coefficient, L is thickness, and k is thermal conductivity of cell material.

Eq. (11) was based on the lumped mass approximation (i.e., uniform cell temperature) due to the low cell Biot number ($\mathrm{Bi} \ll 1$). Moreover, the quasi-steady state approximation was used because of the low Bi and high thermal diffusivity (D_{th}) of the cells (see Subsection 4.1). In this case, the fast thermal responses can be in a state of dynamic equilibrium, and their time derivatives can be close to zero.

3.3. Electrode preparation and pouch cell assembly

An ink slurry for porous activated carbon electrodes was prepared based on the mass weight ratio of 80%:10%:10% by activated carbon (PO0198, MSE Supplies):carbon black, acetylene, 50% (Thermo Fisher Scentific):Carboxymethyl Cellulose (CMC) (Sigma-Aldrich). The slurry was suspended in deionized water (Type II), and was mixed using a centrifugal mixer (SpeedMixer, Flack-Tek, Inc). A doctor blade was set to 50 µm and was used to cast the slurry onto an aluminum foil current collector (50 µm thickness, MSE Supplies). The mass loading of activated carbon electrode material was 10-14 mg cm^{-2}. The electrodes were then dried in a vacuum oven at 100 °C. After drying, the electrodes were punched to the coated area of 24.1 cm^2 (43 mm×56 mm) and were welded with 4 mm width aluminium taps (EQ-PLIB-ATC4, MTI). A cellulose separator (20 µm thickness, Dreamweaver Gold) was sandwiched by two fabricated electrodes for each cell, and the assembly was sealed dry under vacuum, with 1 ml electrolyte added just prior to cell testing. Table 1 summarizes electrode-electrolyte compositions studied.

Table 1: Material compositions for 24.1 cm^2 pouch type cells studied.

Electrode	Solvent[Mass Fraction]	Salt	Concentration
AC-AC[a]	Water[1.0]	$NaClO_4$	5 M
AC-AC	Water[1.0]	$CaCl_2$	1 M
AC-AC	Water[1.0]	$NH_4H_2PO_4$	1 M
AC-AC	Water[1.0]	LiCl	1 M
AC-AC	Water[0.5]/Ethanol[0.5]	LiCl	1 M
AC-AC	Water[0.07]/Ethanol[0.76]/Methanol[0.17]	LiCl	1 M

[a] Activated Carbon-Activated Carbon.

3.4. Electrochemical characterization

A multichannel cycler (Arbin Instrument) was used to evaluate the electrochemical performance of the prototyped cells. The galvanostatic currents were chosen between 20-40 mA, corresponding to the current densities of 8.3-16.6 A m^{-2}. The surface area of the electrode material was used to normalize the currents. The maximum upper and minimum lower cut-off voltages of the cells were selected as 0-1.2 V, that was determined by the range of current-voltage curves showing linear profiles during charging and discharging. During galvanostatic cycling, constant currents were applied to the cells until reaching the upper and lower cut-off voltages with 0.01 V interval. The capacitance (C) of the prototyped cells is calculated using Eq. (12).

$$C = \frac{It_{\mathrm{d}}}{\Delta V} \tag{12}$$

where I is current, ΔV is discharge voltage drop (without IR drop), and t_{d} is discharge time.

The internal resistance of the cells (R) is obtained by the voltage difference right after and before at the end of the charging step, as given by Eq. (13) [37].

$$R = \frac{\Delta V}{I} \tag{13}$$

3.5. X-ray nano-computed tomography and 3D image analysis

Samples were prepared by punching an electrode disk of approximately 1.5 mm in diameter, and were mounted on a stainless-steel dowel with coated surface facing outward using fast-setting epoxy. The sample dowel was then placed into a laser micro-machining system (A Series/Compact Laser Micromachining System, Oxford Lasers, Oxford, UK) to fabricate an electrode pillar with a diameter of approximately 70 µm. The electrode pillar was scanned based on a lab-based X-Ray Nano-Computed Tomography (Nano-CT) system (Zeiss Xradia Ultra 810 X-ray microscope, Carl Zeiss, CA, USA). The instrument was operated based on an isotropic voxel size of 128 nm and a field of view of 64 µm×64 µm. A quasi-monochromatic X-ray beam with an emission energy of 5.4 keV was used for scanning. 901 angular increment radiographs with an exposure time of 20 s were collected over 180° rotation. The radiographs were automatically reference corrected, and were manually center aligned. The corrected and aligned radiographs were reconstructed using Zeiss Advanced Reconstruction Toolbox (Carl Zeiss, CA, USA). The reconstructed 3D volume image was imported into Dragonfly's software (Comet Technologies Canada Inc., Montreal, Canada) [38] for image post-processing.

The electrode porosity (ϵ) is calculated by using Eq. (14).

$$\epsilon = \frac{\text{Total Macropore Volume}}{\text{Total Volume}} \tag{14}$$

Surface area to volume ratio (SA:V) is defined as Eq. (15).

$$\text{SA:V} = \frac{\text{Total Particle Surface Area}}{\text{Total Volume}} \tag{15}$$

TauFactor software [39] was employed to calculate the tortuosity factor of electrodes (τ).

3.6. Specific heat capacity measurements

Differential scanning calorimetry (DSC) Q100 (TA instrument) was used to measure the specific heat capacity of the pouch cell materials, including dry activated carbon electrode, separator, and polymer cell case. The DSC Q100 operated in the temperature range from 16 °C to 80 °C, with heating at a

rate of 2 °C min^{-1} under nitrogen purging. The upper cut-off temperature was determined based on the temperature limit of the cell case that melts above 80 °C. The sample masses were 5-10 mg, which was prepared from a dry pouch cell. The specific heat capacity of aqueous electrolyte was assumed to be the same as that of water, which was calculated using CoolProp 6.4.3 [40]. The specific heat capacity of mixed electrolytes was calculated using mixtures in REFPROP version 10.0 [41]. For example, the specific heat capacity of a mixture with the mass weight ratio of 7%:76%:17% by water and ethanol and methanol is 2.74 J g $°C^{-1}$.

By mass-averaging the specific heat capacities of the cell materials, the effective specific heat capacity of the cell ($c_{p,eff}$) is calculated by Eq. (16).

$$c_{p,eff} = \sum_{i} y_i c_{p,i} \tag{16}$$

where y is mass faction of each material, and constituent i denotes elec (electrode), electrolyte, case (pouch cell case), and sep (separator), respectively. A digital scale (OHAUS Explorer Scale) with the accuracy of ±0.0001 g was used to measure the mass of each cell constituent.

3.7. Thermal diffusivity measurements

Average thermal diffusivities including activated carbon electrodes and a separator were measured using a Discovery Xenon Flash (DXF-500) instrument. The sample masses were 5-10 mg, which was prepared from dry pouch cells. The samples' temperatures were recorded using a nitrogen-cooled infrared detector (InSb sensor). The thermal diffusivities of a pouch cell case and aqueous electrolyte were obtained from low-density polyethylene materials [42] and CoolProp 6.4.3 [40], respectively.

By mass-averaging the thermal diffusivities of cell materials, the effective thermal diffusivity of a cell ($D_{th,eff}$) is calculated by Eq. (17).

$$D_{th,eff} = \sum_{i} y_i D_{th,i} \tag{17}$$

3.8. Modeling parts with assumptions

The cell model was developed using COMSOL Multiphysics software version 6.1 [43] based on a porous electrode theory [44]. Table 2 summarizes

Table 2: An equation set used for thermocapacitive cell and system modeling.

Model	Expression	Description
Cell[a,b]	$\frac{\partial c_\mathrm{i}}{\partial t} + \nabla \cdot J_\mathrm{i} = S_\mathrm{i}$, $\sum_\mathrm{i} z_\mathrm{i} c_\mathrm{i} = 0$	* The one-dimensional Nernst-Planck equation and charge conservation to model the transport phenomena of charged ions (c_i) in electrolyte.
	$J_\mathrm{i} = -D_{\mathrm{i,eff}} \nabla c_\mathrm{i} - z_\mathrm{i} u_{\mathrm{m,i,eff}} F c_\mathrm{i} \nabla \phi_\mathrm{l}$	* A species flux (J_i) governed by diffusion ($D_{\mathrm{i,eff}}$) and electric migration ($u_{\mathrm{m,i,eff}}$).
	$S_\mathrm{i} = -\frac{aC}{2 n_\mathrm{e} F} \frac{\partial(\phi_\mathrm{s} - \phi_\mathrm{l})}{\partial t}$	* A source term (S_i) to model transient EDL charging and discharging processes in the potential difference across the solid-liquid interface, $\frac{\partial(\phi_\mathrm{s} - \phi_\mathrm{l})}{\partial t}$.
	$j = -\sigma_{\mathrm{s,eff}} \nabla \phi_\mathrm{s} + F \sum_\mathrm{i} z_\mathrm{i} J_\mathrm{i}$	* The Ohm's law to model current densities (j) flowing through the electrolyte as well as electric potential field (ϕ) driving those current densities.
	$(m c_\mathrm{p})_\mathrm{eff} \frac{\partial T}{\partial t} = \nabla \cdot (k \nabla T) + \underbrace{I^2 R}_{\dot{Q}_\mathrm{irr}} + \underbrace{\alpha_\mathrm{rev} I T}_{\dot{Q}_\mathrm{rev}} + \underbrace{U A (T - T_\infty)}_{\dot{Q}_\mathrm{amb}}$	* A heat equation with irreversible ($\dot{Q}_\mathrm{irr}$), reversible heat generation rates ($\dot{Q}_\mathrm{rev}$), and heat loss to the ambient ($\dot{Q}_\mathrm{amb}$).
System[c,d,e]	$V = \int_0^a \frac{I}{C} dt$, $W = \int_0^a IV dt$	* Cell voltage and electric energy.
	$T_\mathrm{even} = T_\mathrm{avg} + \frac{Q_\mathrm{chg}}{(m c_\mathrm{p})_\mathrm{eff}}$, $T_\mathrm{odd} = T_\mathrm{avg} + \frac{Q_\mathrm{dischg}}{(m c_\mathrm{p})_\mathrm{eff}}$	* Even index cells charging, odd index cells discharging.
	$T_\mathrm{avg} = \frac{T_\mathrm{even} + T_\mathrm{odd}}{2}$	* Odd index cells contact adjacent even cells with lower index.
	$T_\mathrm{even} = T_\mathrm{avg} + \frac{Q_\mathrm{dischg}}{(m c_\mathrm{p})_\mathrm{eff}}$, $T_\mathrm{odd} = T_\mathrm{avg} + \frac{Q_\mathrm{chg}}{(m c_\mathrm{p})_\mathrm{eff}}$	* Even index cells discharging, odd index cells charging.
	$T_\mathrm{avg} = \frac{T_\mathrm{even} + T_\mathrm{odd}}{2}$	* Even index cells contact adjacent odd cells with lower index.

Notes:

[a] Subscript i denotes species i; (s) and (l) are solid and liquid phase, respectively.

[b] $D_{\mathrm{i,eff}} = \frac{\epsilon}{\tau} D_\mathrm{i}$; $u_{\mathrm{m,i,eff}} = \frac{D_{\mathrm{i,eff}}}{RT}$; $\sigma_\mathrm{eff} = \frac{\epsilon}{\tau}\sigma$; $\frac{1}{U} = \frac{1}{h} + \frac{L_1}{k_1} + \frac{L_2}{k_2}$.

[c] a denotes charging or discharging time; $I > 0$ for charging, $I < 0$ for discharging.

[d] T_even, T_odd, and T_avg: temperatures for even and odd index cells; average temperatures.

[e] Q_chg, Q_dischg: total heat delivered at charged and discharged states, respectively.

the governing equations of the cell model. Main assumptions were (i) one-dimensional species transport, (ii) species flux governed by diffusion and

electric migration, (iii) symmetric binary electrolyte, and (iv) homogeneous volumetric heat generation rates within the electrodes.

The one-dimensional Nernst-Planck equation and effective medium theories (i.e., macrohomogeneous volume averaging) were used to model the transport phenomena of charged ions (c_{i}) in electrolyte. This physics interface was selected due to the model capable of representing significant concentration gradients of ionic species near electrodes [43]. It was assumed that diffusion ($D_{\mathrm{i,eff}}$) and electric migration ($u_{\mathrm{m,i,eff}}$) are dominant transport mechanisms due to the zero flow velocities in the enclosed cells.

The capacitance of the cells was modeled using a source term (S_{i}) representing transient EDL charging and discharging processes in the potential difference across the sold-liquid interface, $\frac{\partial(\phi_{\mathrm{s}}-\phi_{\mathrm{l}})}{\partial t}$ [44]. aC (in F m^{-3}) is volumetric capacitance that varies as a function of current density (j), which was obtained by numerical fitting to the measured currents and voltages. The Nernst-Planck equation was coupled with the Ohm's law to describe current densities flowing through the electrolyte as well as electric potential field driving those current densities.

It was assumed that EDL processes are dominant mechanisms for storing electric charges. This was because the prototyped electrodes were made of activated carbon material, not made of transition metal oxide that could introduce electrochemical reactions [45]. Moreover, the impacts of the insertion of charged ions into the activated carbon electrodes were not explicitly modeled. Instead, volumetric capacitance (aC) was used to model equivalent capacitance capturing both the EDL and Faradaic processes [44].

A thermal model of the cells was developed based on a heat equation with irreversible, reversible heat generation rates, and heat losses to the ambient. The heat equation was coupled with the Nernst-Planck equation to capture resistive heating and heat losses during galvanostatic cycling. The irreversible heat generation rate is predicted by Eq. (18).

$$\dot{Q}_{\mathrm{irr}} = I^2 R \tag{18}$$

where R is cell ohmic resistance. The reversible heat generation rate is modeled using the thermopower of supercapacitors, as expressed by Eq. (19).

$$\dot{Q}_{\text{rev}} = \alpha_{\text{rev}} IT \tag{19}$$

The heat loss to the ambient is predicted by Newton's law of cooling, Eq. (20).

$$\dot{Q}_{\text{amb}} = UA(T - T_{\infty}) \tag{20}$$

To assess the impacts of multiple cells on the overall temperature span, a cascaded cell system model was developed based on Python [46]. Table 2 summarizes the governing equations of the model.

Depending on the operating conditions, the computation time of the multiphysics cell model was a few seconds to minutes, which could result in a thermodynamic cycle simulation time of 10-20 min. To improve the cycle computational efficiency, a lumped-element thermal model was used for each cell model in the cascaded system. This results in the improvement of cycle computational efficiency from 10-20 min to 1-10 s.

The main assumptions for the simplified cell model were (i) negligible self-discharge, (ii) linear voltage profile, (iii) uniform cell temperature, and (iv) cell temperature reaching rapid thermal equilibrium after contacting adjacent cells. The reasons for the assumptions of the (iii) and (iv) were due to the low cell Bi and high D_{th} (see Subsection 4.1 for details).

Total heat generated and released at charged and discharged states are predicted by Eq. (21) and Eq. (22), respectively.

$$Q_{\text{chg}} = \int_0^{t_{\text{c}}} \left(I^2 R + \alpha_{\text{rev}} IT + UA(T - T_{\infty}) \right) dt, \quad \text{where } I > 0 \tag{21}$$

$$Q_{\text{dischg}} = \int_0^{t_{\text{d}}} \left(I^2 R + \alpha_{\text{rev}} IT + UA(T - T_{\infty}) \right) dt, \quad \text{where } I < 0 \tag{22}$$

Cell temperatures at charged or discharged states are calculated by Eq. (23).

$$T = T_{\text{avg}} + \frac{Q_{\text{chg or dischg}}}{(mc_{\text{p}})_{\text{eff}}} \tag{23}$$

where T_{avg} is average cell temperatures of adjacent cells that made contact during the previous cycle stage. The initial T_{avg} was the same as an isothermal bath temperature of 30 °C and changed during charging-discharging steps. T_{avg} is calculated by Eq. (24).

$$T_{\text{avg}} = \frac{T_{\text{even}} + T_{\text{odd}}}{2} \tag{24}$$

where T_{even} and T_{odd} are temperatures for even and odd index cells in contact, respectively.

The log mean temperature difference is particularly useful when the temperature difference across a fluid-based heat exchanger is not constant. A TCHP heat exchanger is based on a fully solid-state regenerator that consists of multiple cells arranged in series, where each cell has a uniform temperature due to cell Bi $\ll 1$. In this case, the arithmetic mean temperature can provide a reasonable approximation of the mean temperature when the heated and cooled cells are in contact with each other.

3.9. Performance evaluation metrics

Temperature span is defined as Eq. (25).

$$\Delta T_{\text{span}} = T_{\text{h}} - T_{\text{c}} \tag{25}$$

where T_{h} and T_{c} are heated and cooled cell temperatures, respectively. When predicting the overall ΔT_{span} of the cascaded system, T_{h} and T_{c} are hot side (right end) and cold (left end) cell temperatures, respectively. The T_{h} is initially the same as T_{c} (ambient temperature) and rises through thermocapacitive cycling.

Total heating delivered (Q_{tot}, in J) from a cold cell to a hot cell is predicted by Eq. (26).

$$Q_{\text{tot}} = (mc_{\text{p}})_{\text{eff}} \Delta T_{\text{span}} \tag{26}$$

where $(mc_{\text{p}})_{\text{eff}}$ is heat capacity of a single cell. Volumetric heating density ($\dot{q}_{\text{v}}$, in kW m^{-3}) is predicted from Eq. (27).

$$\dot{q}_{\mathrm{v}} = \frac{Q_{\mathrm{tot}}}{t_{\mathrm{cd}} V_{\mathrm{volume}}} \tag{27}$$

where V_{volume} is cell volume. Net electric work input (W_{net}, in J) is calculated by the integral of irreversible heating over charging and discharging cycles, as given by Eq. (28). This was based on the assumption that all electric energy losses are converted into Joule heat.

$$W_{\mathrm{net}} = \int_0^{t_{\mathrm{cd}}} I^2 R dt \tag{28}$$

Coefficient of performance (COP) is defined as Eq. (29).

$$\mathrm{COP} = \frac{Q_{\mathrm{tot}}}{W_{\mathrm{net}}} \tag{29}$$

Energy storage density (ED, in kWh m^{-3}) is given by Eq. (30).

$$\mathrm{ED} = \frac{CV^2}{2V_{\mathrm{volume}}} \tag{30}$$

4. Results and Discussion

4.1. Pouch cell fabrication results

Figure 3(A) shows a 24.08 cm^2 (56 mm×43 mm) prototyped cell, which was fabricated to fit between the calorimeter Cu heat spreaders having an area of 36 cm^2. Figure 3(B) illustrates a schematic of a cross-section view of the cell. The entire cells are sealed with polymer cell cases (40 µm) to reduce the heat loss to the ambient. The cell has a total thickness of ∼640 µm including an activated carbon electrode of nearly 250 µm, corresponding to the mass loading of 13.5 mg cm^{-2}.

Figure 3(C) shows the 3D and cross-section images of porous electrode's microstructure measured from X-ray nano computed tomography (nano-CT). The volume averaged porosity (ϵ) is 0.4, and the surface area to volume (SA:V) ratio is 1.5 $\mu\mathrm{m}^{-1}$ (see Supplemental Note S2 for details). The averaged pore size (1.5 µm) is smaller than the average thickness of the electrodes

(250 µm), which validates the use of the porous electrode theory for the capacitor modeling [44]. The tortuosity factor (τ) is 3.6, which decreases the diffusion coefficient (D) and electrical conductivity (σ) of the cells by a factor of nearly 10, predicted by $D_{\text{eff}} = (\epsilon/\tau)D$ and $\sigma_{\text{eff}} = (\epsilon/\tau)\sigma$, respectively [44].

Figure 3(D) displays the breakdown of the thermal mass (mc_{p}) of the prototyped cells. The effective cell thermal mass $(mc_{\text{p}})_{\text{eff}}$ is nearly 5.5 J $^{\circ}\text{C}^{-1}$, which is calculated from the measured mass (m) and specific heat capacities (c_{p}) (see Figure S3 in Supplemental Note S3). The effective heat capacity of the cells ($c_{\text{p,eff}}$) is 2.7 J g^{-1} $^{\circ}\text{C}^{-1}$ by mass-averaging the measured specific heat capacities of their constituents (Eq. (16)). Aqueous electrolyte accounts for 74% of the total $(mc_{\text{p}})_{\text{eff}}$. This is due to 2-4 times higher c_{p} of water (i.e., 4.2 J g^{-1} $^{\circ}\text{C}^{-1}$) than that of the other cell materials.

Figure 3(E) shows that the effective thermal diffusivity ($D_{\text{th,eff}}$) of the cells is 0.145 cm^2 s^{-1} by mass-averaging the measured or calculated D_{th}s of the individual materials (see Table S2 in Supplemental Note S3). The mass-averaging approach was used because of the prototyped cells having simple layered materials which can be treated as a 1-D heat transfer problem. The $D_{\text{th,eff}}$ is 100 times higher than that of aqueous electrolyte due to those accounting for porous electrode structures, but nearly 10 times lower than aluminium foils because of the influence of activated carbon coated.

The prototyped cells have the low Bi of 0.01, which was calculated by hL_{c}/k. h is convective heat transfer coefficient, L_{c} is characteristic length, and k is thermal conductivity. h was assumed to be 5 W m^{-2} $^{\circ}\text{C}^{-1}$ representing the condition of natural convection in air [47]. L_{c} was 600 µm which was obtained from the averaged thickness of the cells. k was 0.28 W m^{-1} $^{\circ}\text{C}^{-1}$ which was obtained from literature representing an effective thermal conductivity for the electrode materials soaked in the aqueous electrolyte [48].

Considering that the cells have Bi $\ll 1$ and high D_{th}, it is reasonable to use the lumped-element model and the quasi-steady state approximation to predict the cell temperature during cycling. In this case, the cell temperature can assume to be uniform and rapidly changes in response to the change in heat generation rates.

Figure 3(F) displays the cyclic voltammetry (CV) results experimentally measured at various scan rates to understand the capacitive processes of

a symmetric cell with 1 M LiCl in water. Two electrode systems with an anode and cathode were used to measure the cell voltage. IR compensation was applied to the CVs. The symmetric shapes are observed and the shape of the CV become more rectangular at lower scan rates. Those results indicate that the cells follow clear capacitive processes during charging and discharging. A deviated CV behavior from an ideal rectangular profile is due

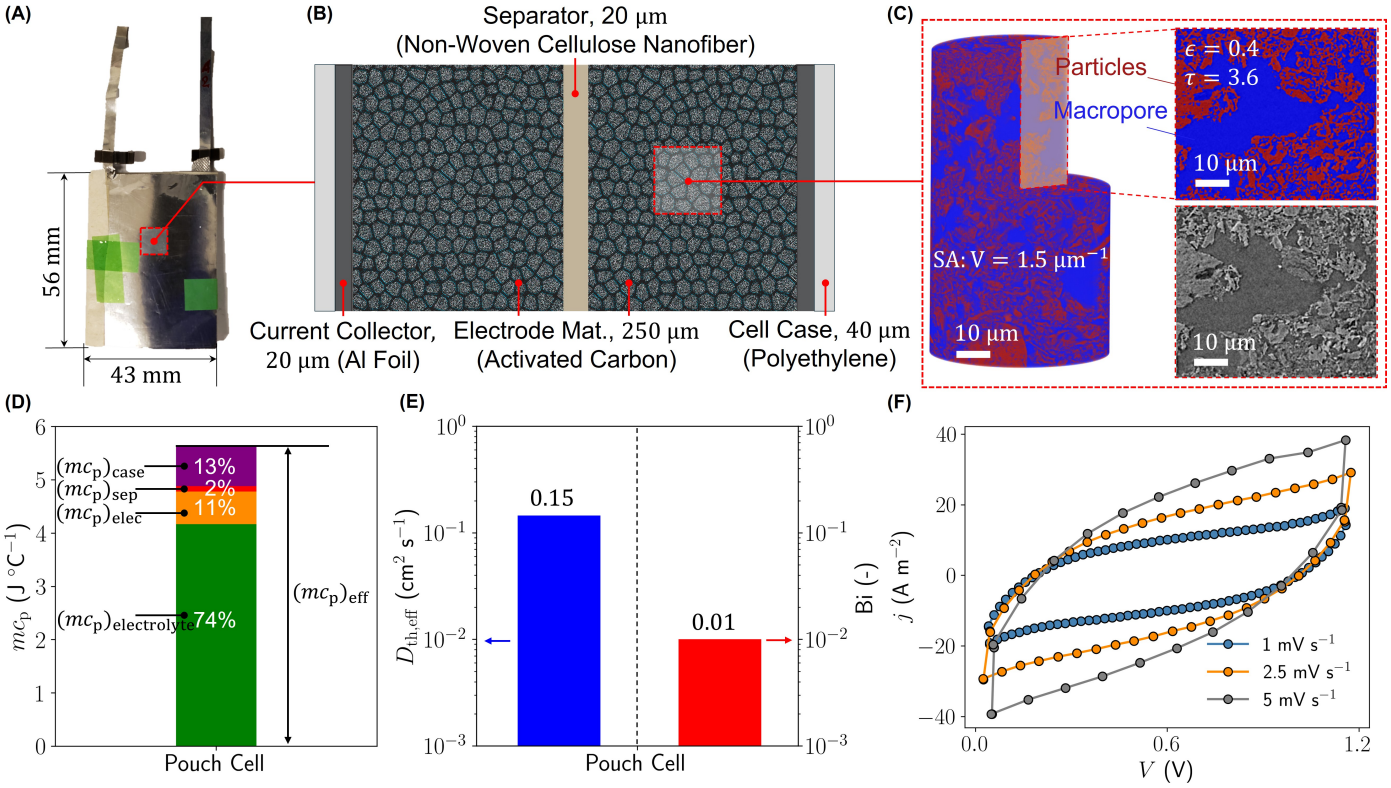

Figure 3: Pouch cell fabrication results. (A) An image of prototyped pouch cell with 24.08 cm^2 (56 mm×43 mm). (B) A schematic of a cross-section view of the cell. (C) A X-ray nano-CT image showing a magnified slice of the activated carbon electrodes showing 2D macro-pores (blue) and particles (red). The solid and liquid porosities (ϵ_s, ϵ_l) and tortuosity (τ_s, τ_l) of the electrode were calculated. (D) Breakdown of thermal mass (mc_p) of the cell using aqueous electrolyte. (E) Effective thermal diffusivity ($D_{th,eff}$) and Biot number (Bi) of the cell using aqueous electrolyte. (F) Cyclic voltammetry (CV) curves experimentally measured at different scan rates based on a symmetric cell with 1 M LiCl aqueous electrolyte. The cell voltages were measured between two electrode systems with an anode and cathode. IR compensation (R = 1.2 Ω obtained from electrochemical impedance spectroscopy of Supplemental Note S5) was applied to the CV curves.

to the Faradaic processes and ohmic resistance. The Faradaic behaviors is expected be arised from the interaction of Li^+ ion with anionic functional groups of carboxymethyl cellulose (CMC) binder [35].

4.2. Temporal evolution of heat generation rate and temperature during galvanostatic cycling

Figure 4 shows the temporal evolution of heat generation rate and temperature of the LiCl aqueous cell during galvanostatic charging and discharging at 8.3 A m^{-2} (left) and 12.5 A m^{-2} (right) between 0-1.2 V. The results show that the measured heat generation rates and temperature profiles at each electrode immediately responded after transitioning from charging to discharging steps (or vice versa). These results indicate that the calorimeter can reasonably quantify the transient heat and temperature profiles of the cells during cycling.

Figure 4(A) and (B) present the temporal evolution of the area-normalized heat generation rates at the positive electrode ($\dot{q}_+$), at the negative electrode ($\dot{q}_-$), and in the entire cell ($\dot{q}_T$). The total heat generation rates are calculated by the sum of the heat generation rates at each electrode. The measured heat rates are oscillated during the galvanostatic cycling due to the change in total reversible heat generation rates ($\dot{q}_{T,rev}$).

The peak reversible $\dot{q}_{T,rev}$ decreases at the higher currents from 3.8 W m^{-2} to 1.6 W m^{-2} due to the faster charging and discharging processes leaving more unused area and energy in the capacitive devices. This is indicated by the reduced cell capacitance from 5.8 F to 3.5 F. Moreover, the faster charging and discharging rates yield increase in irreversible $\bar{q}_{T,irr}$ from 4 W m^{-2} to 7.4 W m^{-2} due to Joule heating that is caused by ohmic resistance of 13 Ω in the capacitor.

The thermal behavior of each electrode in the LiCl aqueous capacitor occurs in asymmetric manner. This leads to the LiCl cell cooling down as charging, and heating up as discharging. As charging, Li^+ ions move to the negative electrode (gray markers) and they absorbs energy from surroundings to overcome a potential barrier, resulting in electrolyte cooling [49]. Whereas, Cl^- ions move to the positive electrode (orange markers), it forms EDL and generates heat. Because the heat changes caused by the insertion of Li^+ ions into the electrodes dominate the cell heating, cooling (heating) occurs as charging (discharging).

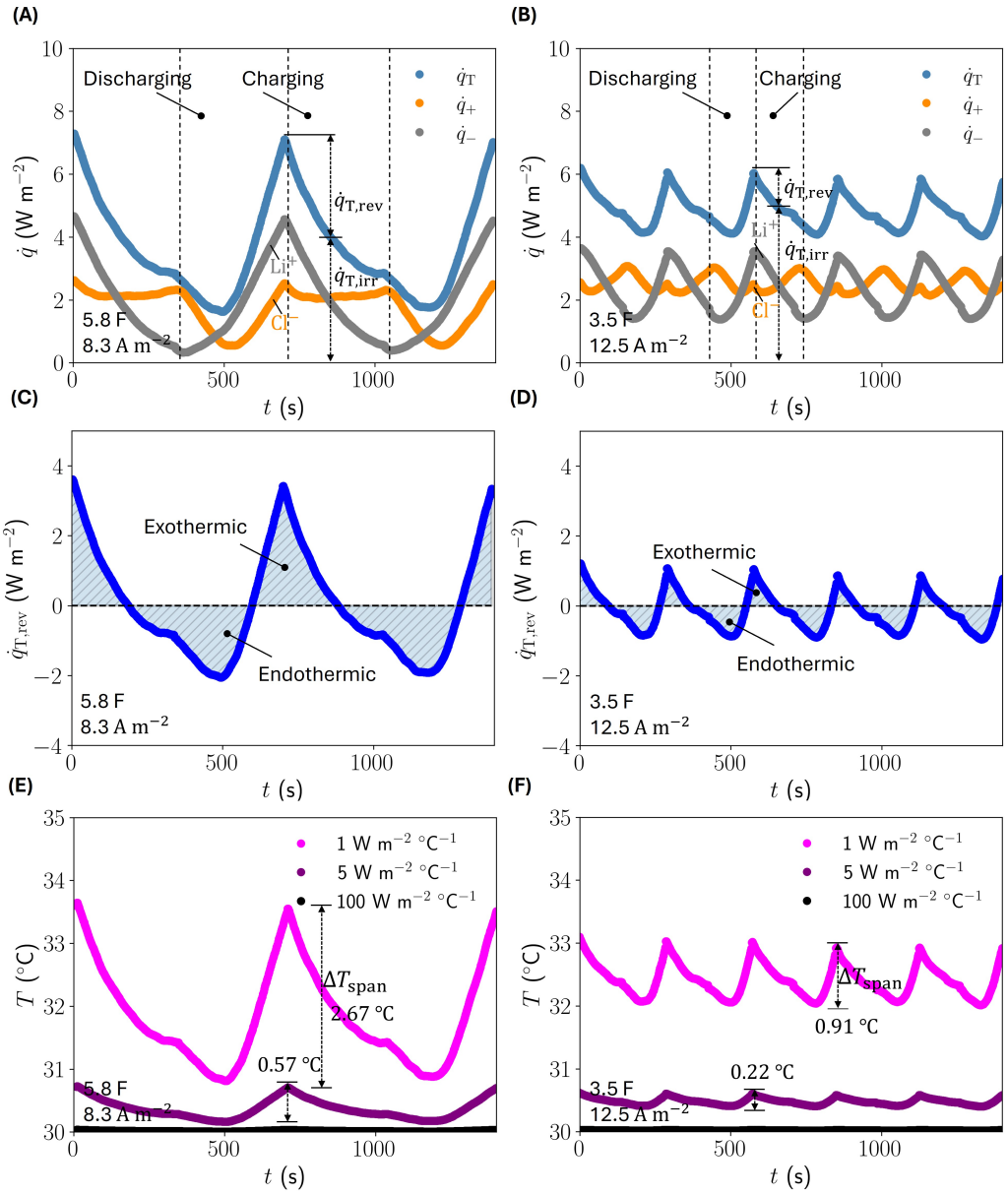

Figure 4: Calorimetry results. Galvanostatic cycling is performed at 8.3 A m^{-2} (left) and 12.5 A m^{-2} (right) between 0-1.2 V based on a symmetric cell with 1 M LiCl aqueous electrolyte. (A) and (B) Each solid line represents the area-normalized heat generation rates: total $\dot{q}_{\mathrm{T}}$ (steelblue), positive electrode $\dot{q}_{+}$ (orange), and negative electrode $\dot{q}_{-}$ (grey). Total $\dot{q}_{\mathrm{T}}$ is sum of $\dot{q}_{+}$ and $\dot{q}_{-}$. Each $\dot{q}$ consists of reversible ($\dot{q}_{\mathrm{T,rev}}$) and irreversible ($\dot{q}_{\mathrm{T,irr}}$) heat generation rates. (C) and (D) Time-dependent reversible heat generation rates. (E) and (F) Projected cell temperature profiles in response to heat generation rates at different overall heat transfer coefficients.

Figure 4(C) and (D) illustrate that $\dot{q}_{T,rev}$ is symmetric exothermic and endothermic processes. The heat energy produced during charging and discharging cycles is recovered when the process is reversed. This phenomena is originated from the redox reactions and ion adsoprtion/desoprtion processes.

$\dot{q}_{T,rev}$ can be linked to the thermopower of cells by $\dot{q}_{T,rev} = \alpha_{rev} jT$. α_{rev} is equivalent to an effective Seebeck coefficient (in mV $^{\circ}C^{-1}$) for electrochemical cells, which describes a material's ability to generate heat from electric currents (or vice versa) through the entropy changes of the cells [18].

The decrease in the peak $\dot{q}_{T,rev}$ at the higher currents from 3.8 W m^{-2} to 1.6 W m^{-2} corresponds to the decrease in the averaged α_{rev} from -1.7 mV $^{\circ}C^{-1}$ to -0.65 mV $^{\circ}C^{-1}$. The negative sign reflects heat absorptions during charging. Given the fact that the cell capacitance reflects the number of ions involving with electrolyte entropy changes, the decrease in the cell capacitance from 5.8 F to 3.5 F at the higher currents yields the lower specific entropy change (Δs) from 45.5 J kg^{-1} $^{\circ}C^{-1}$ to 1.7 J kg^{-1} $^{\circ}C^{-1}$ and thus reduced the $\dot{q}_{T,rev}$ and α_{rev}.

Since the calorimeter was designed to quantify the heat fluxes from cells, an equivalent thermal circuit was used to predict the temperature of the cells (Eq. (11)). Figure 4(E) and (F) show the projected cell temperature profiles in response to heat generation rates with different overall heat transfer coefficients (U). When U is 1 W m^{-2} $^{\circ}C^{-1}$, the cell temperature span (ΔT_{span}) is 0.9°-2.7 °C. When U is 5 W m^{-2} $^{\circ}C^{-1}$, ΔT_{span} is 0.22 °C to 0.57 °C. Those ΔT_{span} are less than 0.03 °C when U is 100 W m^{-2} $^{\circ}C^{-1}$. The decrease in ΔT_{span} at U is a result of larger heat losses to the ambient.

4.3. Cell design factor parametric assessment

The influence of different electrolytes on the performance of the prototyped cells is plotted in Figure 5(A). The mixed solvents were used to assess the influence of organic solution on the change in electrolyte entropy [50]. The measurements were taken at 8.3 A m^{-2}. For direct performance comparison, the average reversible heat generation rate ($\overline{\dot{Q}}_{rev}$) (Eq. (10)) and capacitance (C) are normalized with each dry electrode mass (m_{elec}) (see Table S3 and Figure S4 in Supplemental Note S4 for details on the measured values and anticipated temperature profiles).

The comparison shows that the cell with 1 M LiCl aqueous electrolyte produces relatively both high $\overline{\dot{Q}}_{\text{rev}}\ m_{\text{elec}}^{-1}$ and $C\ m_{\text{elec}}^{-1}$. This is primarily due to the Faradaic processes involved in the LiCl device, enhancing the electrolyte entropy change [49]. The cells with 1 M $CaCl_2$ in water show tradeoff between their higher reversible heat and lower capacitance than the LiCl aqueous cells. This is because $CaCl_2$ has a larger enthalpy of solution (-81.3 kJ mol^{-1}) than that of the LiCl cell (-37 kJ mol^{-1}), but cause nearly 60% larger cell resistance (10.4 Ω) and thus Joule heating.

The cells with mixed solvent electrolytes generally produce lower thermal and electrochemical performance (orange shaded region) than those of the cells with pure water solvent (steelblue shaded region). To be specific, the cells with water/ethanol (the mass weight ratio of 50%/50%) electrolyte produce comparable $\overline{\dot{Q}}_{\text{rev}}\ m_{\text{elec}}^{-1}$ to those of the cells with pure water solvent (steelblue shaded region) but lower $C\ m_{\text{elec}}^{-1}$. This is a result of tradeoff between reduced water content that decreases in cell capacitance by 33% and the increased cell thermopower (specific entropy change) by 5%. The water/ethanol cell temperature span is 0.62 °C higher than the pure water solvent cell due to the reduced density and specific heat capacity of the solvent mixture relative to pure water.

The cells using water/methanol/ethanol (the mass weight ratio of 7%:76%:17%) electrolyte produces lower $\overline{\dot{Q}}_{\text{rev}}\ m_{\text{elec}}^{-1}$ and $C\ m_{\text{elec}}^{-1}$ than the others. This is because the significant reduced water contents decreases the ionic conductivity of the cells, which causes higher cell ohmic resistance and Joule heating. For example, a LiCl cell resistance was increased from 6.5 Ω to 30 Ω when changing the solvent from water to mixed solvents. Balancing water content with the composition of a mixed-solvent electrolyte is crucial for improving the performance of thermocapacitive cells, particularly in enhancing their reverisble heat and capacitance.

Figure 5(B) shows the performance comparison of a LiCl aqueous cell between the measured and modeled data at the current density of 12.5 A m^{-2} and U of 5 W m^{-2} °C^{-1}. For model validations, a symmetric cell with 1 M LiCl aqueous electrolyte was used to assess the accuracy of the multiphysics cell model. Two empirical parameters were obtained from calorimetry data: (i) volumetric capacitance (aC in F m^{-3}) and (ii) α_{rev}. For example, aC is 20.5 F m^{-3} at the current density of 12.5 A m^{-2}, which corresponds to the

volume of active materials in the electrode of 0.34 m^3 for a cell capacitance of 3.5 F. α_{rev} is -0.65 mV $°C^{-1}$, which corresponds to the area-normalized reversible heat generation rate of 0.35 W m^{-2} (see Figure S6 in Supplemental Note S6 for details on the results at different current densities). The mean absolute errors (MAEs) of the heat and temperatures are 0.43 W m^{-2} and 0.03 °C, respectively. Since the modeled heat generation rates are based on the isentropic processes, the deviations are primarily attributed to the irreversible processes including heat losses to the ambient, ohmic heating, and self-discharging [17].

Figure 5(C) shows the results of sensitivity analysis on ΔT_{span} with the range of applied current densities. The blue and red markers with a dashline are the measured and predicted ΔT_{span}, respectively. The MAEs of ΔT_{span}s between the average measured and predicted data is less than 0.01 °C, presenting good agreement. Both measured and modeled ΔT_{span} decreases from 0.56 °C to 0.1 °C at higher currents. This is due to the faster charging and discharging processes that leave more unused area and energy in the capacitive devices, decreasing the cell capacitance from 5.8 F to 2.1 F. If the cell capacitance is reduced by 63%, the cell temperature changes are decreased proportionally by 64%.

Figure 5(D) details the breakdown of heat generation rates at the different applied current densities. For each data point, the time-averaged heat generation rates are normalized with the cell area. The results show that the faster charging and discharging yield increase in the time-averaged irreversible $\overline{\dot{q}}_{T,irr}$ from 4 W m^{-2} to 7.4 W m^{-2} and increase in the ratio of the irreversible $\overline{\dot{q}}_{T,irr}$ to the total $\overline{\dot{q}}_T$ from 58% to 96.5% due to enhanced Joule heating.

Figure 5(E) shows the influence on ΔT_{span} of α_{rev} and $(mc_p)_{eff}$ at 12.5 A m^{-2} and U of 5 W m^{-2} $°C^{-1}$. The x-axis refers to $(mc_p)_{eff}$ and y-axis corresponds to α_{rev}, where the lower and upper bounds are determined based on ±50% variation of mc_p and α_{rev} from the prototyped LiCl cell (yellow marker). The (e,t) denotes the prediction based on experiment data and theory. The color contour represents ΔT_{span} at the charging time of 250 s, where the negative sign refers to temperature drop and positive sign corresponds to temperature lift.

To explain this plot, three different scenarios are illustrated by the black arrows in Figure 5(E), which are discussed below:

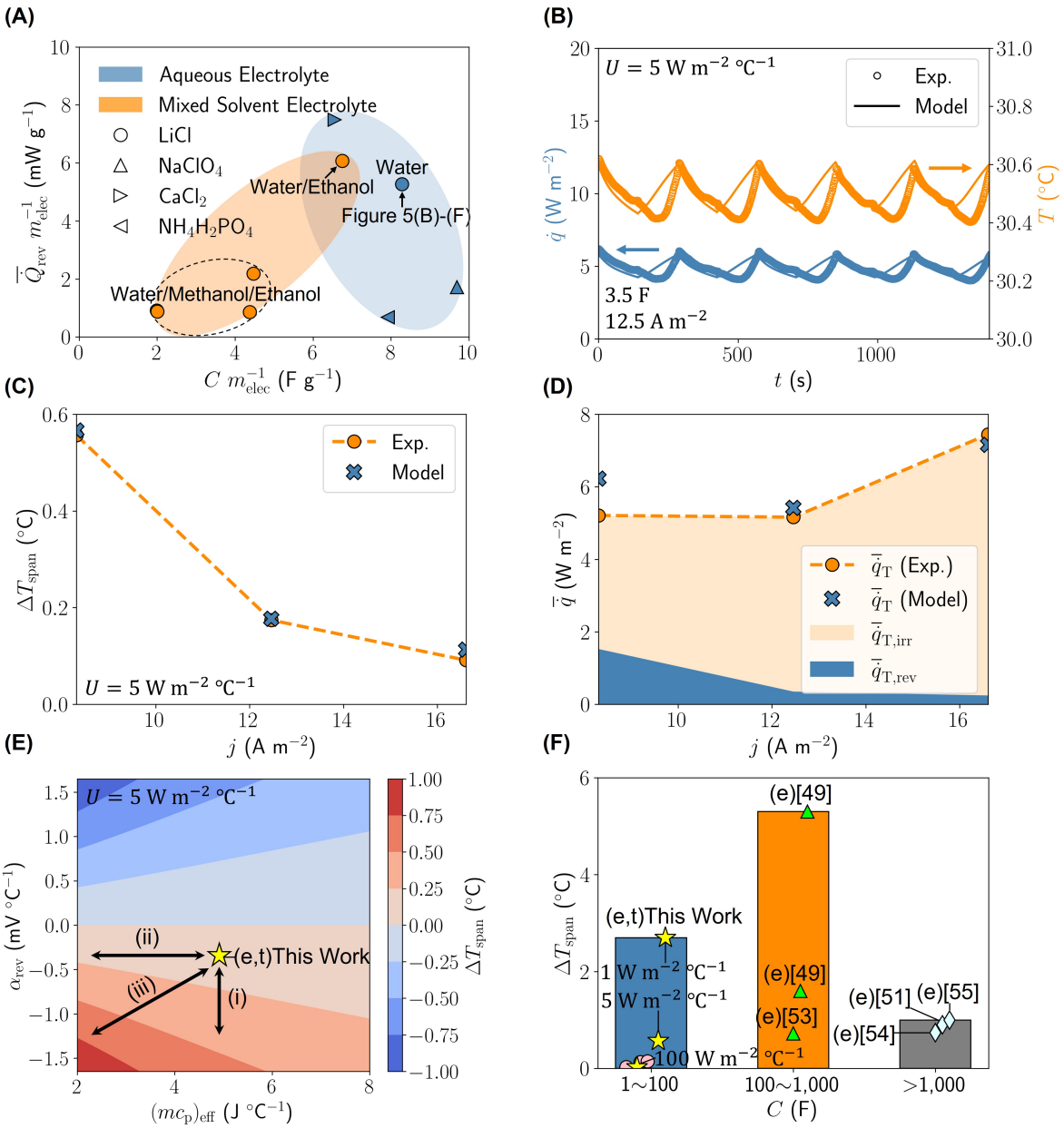

Figure 5: Cell design factor parametric assessment. (A) Performance comparison of the prototyped cells with different electrolytes. (B) Model validation results: temporal evolution of heat generation rate and cell temperature during galvanostatic cycling. (C) Temperature span (ΔT_{span}) as a function of applied current density (j). (D) Breakdown analysis of area-normalized, time-averaged heat generation rates ($\bar{\dot{q}}$) as a function of applied j. (E) The influence of thermopower (α_{rev}) and effective thermal mass ($(mc_{\text{p}})_{\text{eff}}$) on ΔT_{span}. (F) Plot showing reported maximum temperature swings from various supercapacitors [49, 51, 52, 53, 54, 55, 56].

(i) A change in α_{rev} at a constant mc_p: this corresponds to a vertical movement relative to the yellow marker (reference case). The degree of ΔT_{span} can be enhanced from 0.25 °C to 0.75 °C when improving α_{rev} by a factor of 2 for a given mc_p of 2 J °C^{-1}. One of the most recently characterized thermocapacitive cells used aqueous K_2SO_4 electrolyte and carbon-MnO_2 electrodes to generate α_{rev} of 0.3-0.6 mV °C^{-1} [52]. The Faradic reactions involved in the oxide electrode led to 1.3 times higher α_{rev} than that in the carbon electrodes, which improves ΔT_{span} by a factor of 1.5.

(ii) A change in mc_p at a constant α_{rev}: this refers to a horizontal movement in the graph. For instance, the ΔT_{span} can be enhanced from 0.5 °C to 1 °C during 250 s when the cells have 3 times lower mc_p than that of the prototyped ones having 5 J °C^{-1}. This can be achieved by fabricating thinner electrodes, which requires additives to improve electrolyte wetting [57]. Moreover, considering that aqueous electrolyte accounts for nearly 80% of the cell mc_p, the use of organic electrolytes with 2 times lower density (e.g., propylene carbonate, 1.2 g cm^{-3}) can lower mc_p by half and enhance ΔT_{span} by a factor of 2.

(iii) A change in both α_{rev} and mc_p: this relates to a diagonal movement relative to the black marker. By reducing mc_p and improving α_{rev} by a factor of 2, the cells can enhance ΔT_{span} from 0.25 °C to 1 °C. This can be achieved by both fabricating thinner electrodes to reduce inactive mc_p and identifying the optimal combinations of electrolyte-electrode pairings to improve α_{rev}.

Figure 5(F) shows the impacts of U for selected cells and C on ΔT_{span}. The findings of this study are compared with the reported ΔT_{span}s of various supercapacitive cells having low C ($<$ 100 F) [52, 56], medium C (100-1,000 F) [49, 53], and high C ($>$ 1,000 F) [51, 54, 55].

The maximum temperature span of the LiCl cells is 2.7 °C when U = 1 W m^{-2} °C^{-1}, which is higher than other cells designed less than 100 F. The smaller ΔT_{span} of 0.13°-0.57 °C are due to heat losses when U is $>$ 5 W m^{-2} °C^{-1}. The comparison shows that cells can achieve higher ΔT_{span} of 1°-5.8 °C at increased capacitances. This is because the increased number of ions is advantageous to achieve larger electrolyte ΔS. The highest reported change in temperature is 5.8 °C based on a 720 F commercial Li-ion capacitor [49]. The lab fabricated EDLCs show temperature drops less than 1 °C due to

those C below 10 F (see Table S5 in Supplemental Note S7 for details on the data points).

4.4. Prediction of cascaded cell system performance

A cascaded cell system model was used to evaluate the influence of multiple cells on the overall temperature lifts. For model validations, a prototyped symmetric cell with 1 M LiCl aqueous electrolyte was used to examine the accuracy of the simplified cell model used in the heat pump system model.

Figure 6(A) summarizes the result of comparison between the projected amount of reversible heat delivered (Q_{rev}), C, and ΔT_{span} with calorimetry data. The data was obtained from one charging and discharging cycle based on a unit cell. Each parameter was normalized with each average experimental value. The U of 1 W m^{-2} °C^{-1} was assumed to simulate the well-insulated unit operating at ambient temperature. The MAEs of Q_{rev}, C, and ΔT_{span} are 0.04 J, 0.09 F, and 0.09 °C, respectively. This indicates that the cell model can reasonably represent the performance of the thermocapacitive cell in the cascaded system (see Figure S7 in Supplemental Note S6 for details).

Figure 6(B) shows a contour plot representing the influence of the number of cells (N_{cell}) and repeated cycles (N_{cycle}) on the ΔT_{span}. The ranges of N_{cell} and N_{cycle} are determined from an electrocaloric device with multiple cells [27]. The cell geometries and material properties are obtained from the prototyped LiCl cells. The peak ΔT_{span} is nearly 7 °C at 12.5 A m^{-2} when the nine cell and cycles are used. This is because the larger regenerator with the higher cycle frequency can deliver more heat from a cold to a hot side cell than a unit cell, enhancing ΔT_{span}. For example, ΔT_{span} of the nine cascaded cells is 2.2 times higher than that of the three cascaded cells.

Figure 6(C) displays the time evolution of the adiabatic ΔT_{span} and cell temperatures at 12.5 A m^{-2} based on the nine cells and cycles selected. The ΔT_{span} is monotonically increasing as a result of the movement of heat from cold to hot cells during cycling. The peak adiabatic ΔT_{span} is found to be nearly 2,500 s, corresponding to the last cycle. The increase in the ΔT_{span} per cycle is due to the increase in the temperature swing of a cold cell that is contacted with a thermal reservoir of 30 °C as shown in the blue solid line of the plot.

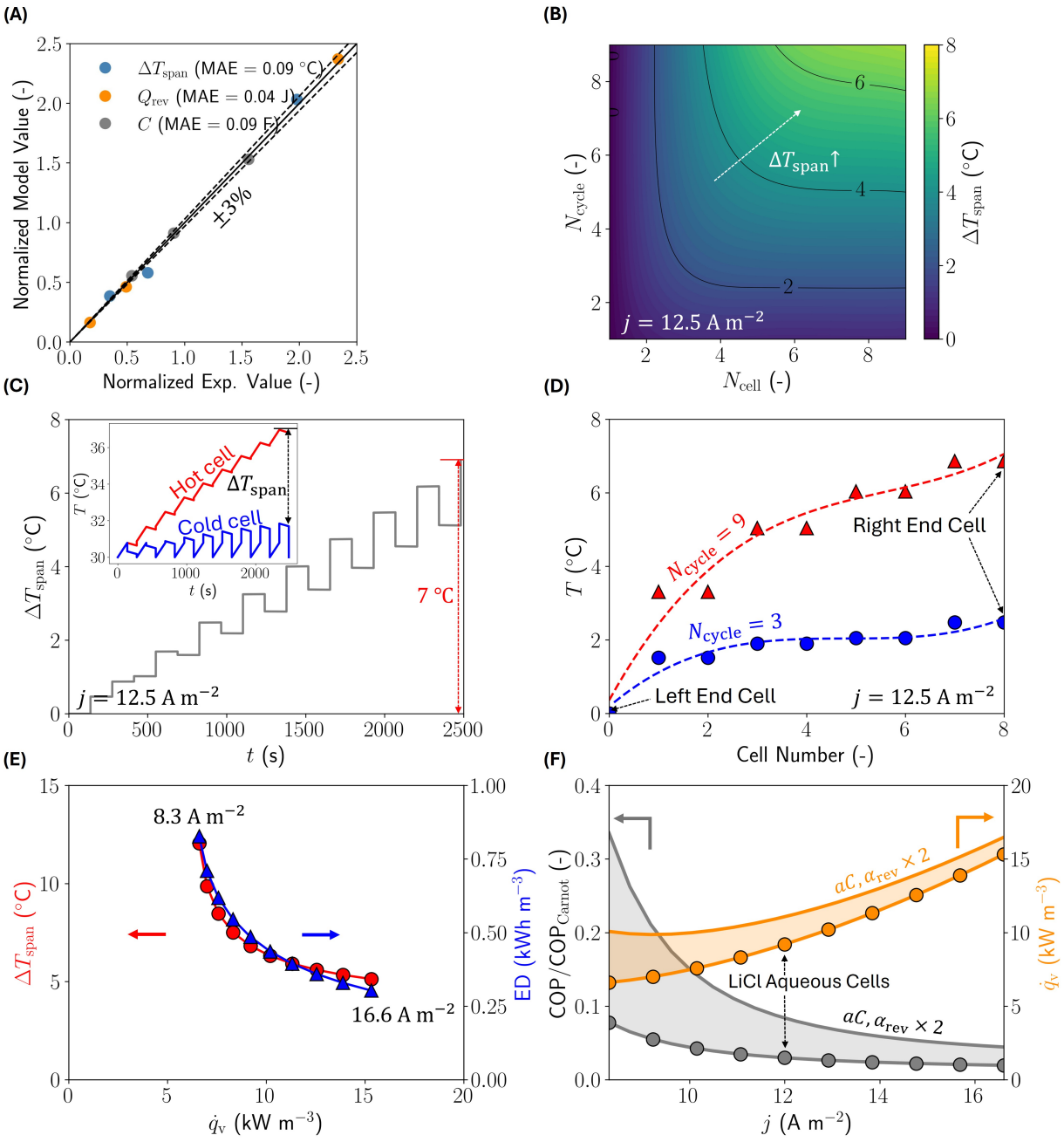

Figure 6: Prediction of cascaded cell system performance. (A) Comparison of modeled unit cell performance parameters with calorimetry data (each parameter is normalized with each averaged experimental value). (B) ΔT_{span} of the cascaded cell system as a function of the number of cells (N_{cell}) and cycles (N_{cycle}) at a fixed j of 12.5 A m^{-2}. (C) Time evolution of ΔT_{span} and temperature of the cell. (D) Temperature distribution of the cascaded cells at the different N_{cycle}. (E) ΔT_{span} and energy storage density (ED) as a function of volumetric heating capacity ($\dot{q}_v$). (F) Predicted COP/COP$_{Carnot}$ and $\dot{q}_v$ as a function of j.

Figure 6(D) presents that the cells in series are cycled through the cell fixture between two reservoirs to gradually build up a temperature difference between the reservoirs. The cold- and hot-side cell temperatures are shown in the left and right end of the plots, respectively. It is clear that the hot cell temperature increases significantly with relative to the cold cell for a given current density. The larger magnitude of temperature distribution across the cascaded cells can be achieved at the higher N_{cycle} when maintaining adiabatic condition.

Figure 6(E) shows the influence of current density on the thermal and energy storage performance of a nine cascaded cell system. Each marker represents ΔT_{span} and energy storage densities (ED) respectively which are both a function of heating density ($\dot{q}_{\text{v}}$). It is clear that ΔT_{span} and ED decrease with increasing heating density. This is a classic tradeoff between capacity and temperature lift in caloric cooling and heating devices.

On the right end of the performance curve, the data shows the maximum $\dot{q}_{\text{v}}$ of 15 kW m^{-3} at the minimum ΔT_{span} of 5 °C and ED of 0.3 kWh m^{-3}. On the left end of the plot, slower charging/discharging will increase the overall ΔT_{span} by up to 12.1 °C and ED of 0.83 kWh m^{-3}. The decrease in capacity at lower current densities is attributed to the increased cycling time which is more significant than the rise in ΔT_{span}.

Higher $\dot{q}_{\text{v}}$ can be achieved via higher current densities due to the reduced cycling time, but it will also lower reversible heat. This is because faster charging/discharging will yield an increase in Joule heating, thus reducing the depth of charge/discharge of thermocapacitive cells (i.e., reduced ion utilization). TCCs are based on electric double layer capacitors (EDLC), which are inherently an energy storage device. For the key attributes of any storage device, there is a trade-off between energy and power characteristics, which is often represented by Ragone plots.

To improve both $\dot{q}_{\text{v}}$ and ΔT_{span}, an ideal system would utilize cells with lower ohmic losses and larger reversible heat at higher current densities. This would reduce the cycling time and associated heat losses and increase the heat delivered per cycle. For example, the TCHPs may provide a potential $\dot{q}_{\text{v}}$ and ΔT_{span} increase of over 30% when the cell resistance is reduced by 50% and thermopower is enhanced by 50% with relative to the prototyped cells.

Figure 6(F) shows a performance map for a TCHP cycle in terms of the second law efficiency (also called exergy efficiency, $\mathrm{COP/COP_{Carnot}}$) as a function of current density. The TCHP can achieve the highest second law efficiency at the lowest current density. The expected peak $\mathrm{COP/COP_{Carnot}}$ is 0.08 (i.e., COP of 2) based on prototyped LiCl aqueous cells (markers). The drop in the system efficiency with increasing the current densities is due to Joule heating, which accounts for 96.5% of total heating at 16.6 A $\mathrm{m^{-2}}$.

The monotonic increase in $\dot{q}_{\mathrm{v}}$ at higher current densities is due to the greater impacts of reduced cycling time than that of the decrease in ΔT_{span}. An optimal current density would be the range of current densities from 8.3 A $\mathrm{m^{-2}}$ to 10 A $\mathrm{m^{-2}}$ that can achieve heating density of 6-8 kW $\mathrm{m^{-3}}$ with relatively high $\mathrm{COP/COP_{Carnot}}$ of 0.1-0.3.

Classic trade-offs between efficiency and power density are often observed in electrochemical refrigeration technologies [58, 59]. As mentioned, higher $\dot{q}_{\mathrm{v}}$s with higher currents will produce an increase in Joule heating and a decrease in the depth of charge/discharge of the cells, decreasing $\mathrm{COP/COP_{Carnot}}$. On the other hand, lower $\dot{q}_{\mathrm{v}}$s with lower currents will produce larger reversible heat and temperature spans, increasing $\mathrm{COP/COP_{Carnot}}$. Heat would be efficiently transferred by absorbing heat when temperatures drop and releasing it when temperatures rise.

The second law efficiency theoretically reaches up to 0.33 as long as the cell achieves two-fold increases in both the aC and α_{rev}. Fabricating cells with larger aC and α_{rev} would be possible due to the recent advancements in supercapacitive cells. The ED of the supercapacitors can reach as high as 60-88 kWh $\mathrm{m^{-3}}$ [21, 22], which is 10 times higher than that of the prototyped LiCl aqueous cells. This means the cell has potentials to enhance aC by a factor of 10. Moreover, an iron-based electrolyte design strategy using a binary solvent and anion engineering produces a high α_{rev} of 3.73 mV $\mathrm{^{\circ}C^{-1}}$ [50], which is 2-3 times higher than that of the prototyped ones.

4.5. Performance comparison of heat pumping and energy storage technologies

Figure 7(A) shows that the findings of this work have been compared with the state-of-the-art caloric heat pumping technologies [27, 58, 60, 61, 62, 63, 64, 65, 66, 67, 68, 69]. The recent research on electrochemical heat pump-

ing [59, 70] has also been included to enable direct performance comparison with the TCHPs. Those comparisons are because the temperature change in the thermocapacitive cell materials is induced solely through the application of electrical potentials, analogous to electrocaloric and electrochemical devices.

The performance comparison is based on three measures for caloric cooling and heating [71]: The maximum $\Delta T_{\mathrm{span,max}}$ (x-axis), $\mathrm{COP_{max}}/\mathrm{COP_{Carnot}}$ (y-axis), and $\dot{q}_{\mathrm{v,max}}$ (color contour). The data shown for electrochemical and caloric materials are typical values based on criteria: (i) measurement taken of adiabatic temperature change and heating/cooling capacity on the same system, (ii) measurement taken near ambient condition, (iii) reversible material changes under the applied driving forces, (iv) chamber volume (or associated geometry) explicitly reported, and (v) the data reported within 10 years. Superscripts (e) and (t) correspond to experimental and theoretical results, respectively.

Although the performance of caloric systems might be varied under a range of different operating conditions, the impact of changes in hot- and cold-side temperatures, thermal boundary conditions, and the size of the system would be less significant in caloric systems for the following reasons:

- The power densities of the reported caloric devices range from 10 to 1000 kW $\mathrm{m^{-3}}$, but their system capacities are mostly less than 300 W. This means that the results are based on laboratory-scale measurements, similar to those of thermocapacitive devices.
- The influence of cold and hot-temperatures on the performance of the caloric device would be less significant than VC technologies. In VC cycles, lower temperature lifts yield higher isentropic efficiency and reduced compressor power, allowing for high $\mathrm{COP_h}$. Caloric heat pumps are compressor-free systems that use liquid pumps to circulate heat transfer fluids. The power of the liquid would not be affected by temperature lifts.
- Measurements in the literature might be taken under "near-adiabatic conditions" due to the use of thick acrylic end plates [59], insulation layers [27], or a combination of these [62]. In addition, the difference in the size of the caloric systems would be small, as indicated by the chamber volumes in Table S6 of Supplemental Note S7. Given that the

collective heat loss is proportional to the exterior area, the influence of the difference in the size on the heat losses would be small.

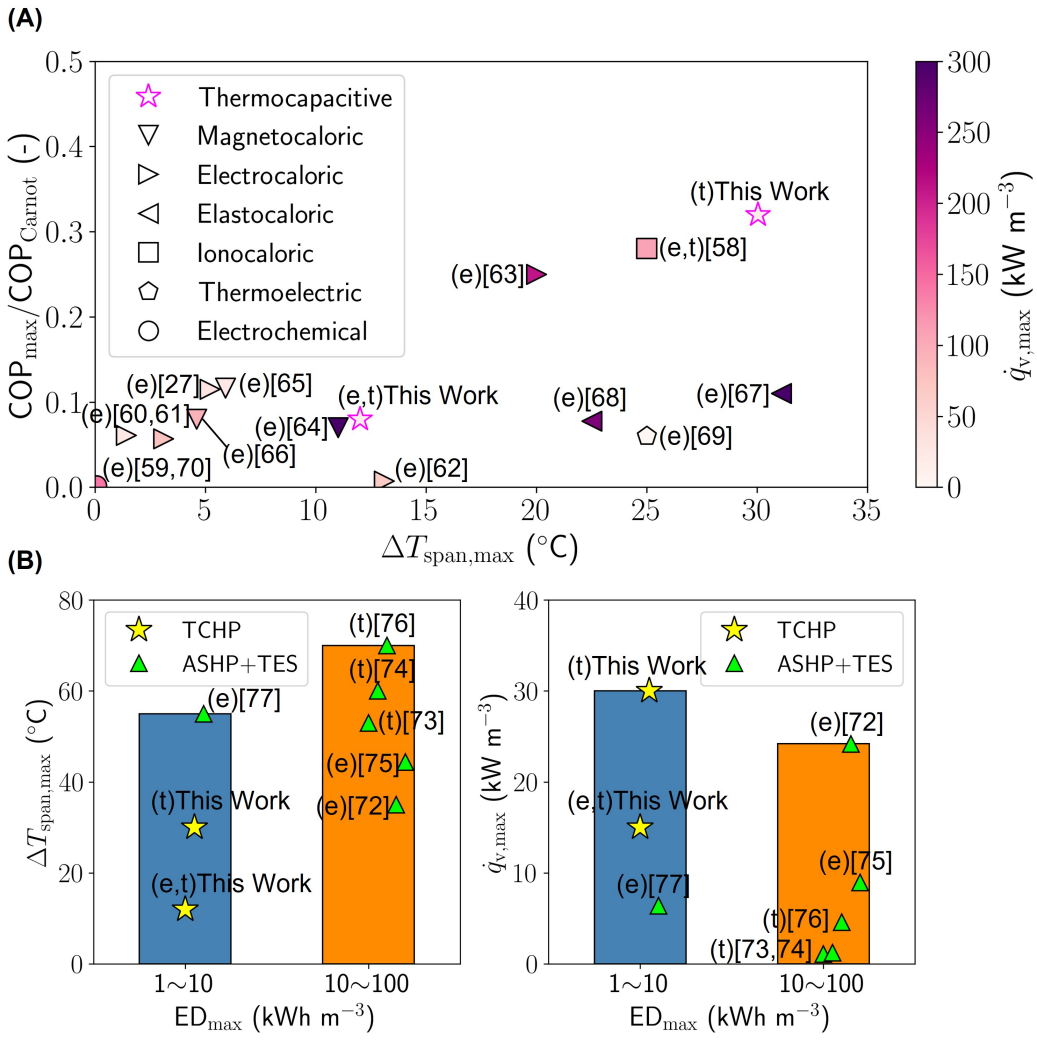

Figure 7: Performance comparison of heat pumping and energy storage technologies. Superscripts (e) and (t) correspond to experimental and theoretical results, respectively (see Table S6 and S7 in Supplemental Note S7 for details on the data). (A) Comparison of COP_{max}/COP_{Carnot}, $\Delta T_{span,max}$, volumetric cooling/heating density ($\dot{q}_{v,max}$) of thermocapacitive, electrocaloric [27, 60, 61, 62, 63], ionocaloric [58], magnetocaloric [64, 65, 66], elastocaloric [67, 68], thermoelectric [69], and electrochemical [59, 70] heating and cooling devices. (B) Comparison of $\Delta T_{span,max}$, ED_{max}, and $\dot{q}_{v,max}$ of TCHPs and air-source heat pump (ASHP) with thermal energy storage (TES) [72, 73, 74, 75, 76, 77].

The TCHP has potential to achieve high second law efficiency while producing comparable $\Delta T_{\text{span,max}}$ to the other caloric devices. Leveraging the prototyped LiCl aqueous cells in a cascaded manner, the projected $\Delta T_{\text{span,max}}$ is 12 °C and $\dot{q}_{\text{v}}$ is 15 kW m^{-3}, both at the U of 1 W m^{-2} °C^{-1}. This $\Delta T_{\text{span,max}}$ is comparable to that of electrocaloric devices based on multilayer capacitors [61, 62], higher than that of magnetocaloric devices showing 5.9-11 °C [64, 65], and superior than that in electrochemical devices showing $\Delta T_{\text{span,max}}$ less than 1 °C [59, 70]. If the aC and α_{rev} of the LiCl cell can be doubled, $\Delta T_{\text{span,max}}$ could theoretically be reached up to nearly 30 °C with $\text{COP}_{\text{max}}/\text{COP}_{\text{Carnot}}$ of 0.33 at 8.3 A m^{-2}. Those projected performance supersedes most of the other caloric and electrochemical heat pumps.

Although a magnetocaloric device using solid-state heat recuperation [66] reported higher theoretical $\text{COP}_{\text{max}}/\text{COP}_{\text{Carnot}}$ of 0.54 and $\Delta T_{\text{span,max}}$ of 26 °C, their experimentally obtained efficiency is 0.08 ($\Delta T_{\text{span,max}}$ of 4.6 °C) which is comparable to the performance using thermocapacitive cells ($\text{COP}_{\text{max}}/\text{COP}_{\text{Carnot}}$ of 0.08, $\Delta T_{\text{span,max}}$ of 12 °C) as shown in Figure 7(A). Most magnetocaloric refrigerators can go higher than 12 °C, but their $\text{COP}_{\text{max}}/\text{COP}_{\text{Carnot}}$ is less than 0.3 [66]. The TCHPs can be one of the alternative technologies which can achieve both high efficiency and temperature spans at low current density and using relatively abundant materials like activated carbon and aqueous electrolytes.

Future works are needed to improve the $\dot{q}_{\text{v}}$ of the TCHPs to meet practical size requirements. For example, the $\dot{q}_{\text{v}}$ of 15 kW m^{-3} of the TCHP is nearly 17-20 times lower than 160-300 kW m^{-3} of elastocaloric heat pumping [68, 78], nearly 9.4 times lower than 140.6 kW m^{-3} of electrochemical cooling [59], and nearly 7.3 times lower than 110 kW m^{-3} of ionocaloric cooling [58]. One of the ways to produce higher $\dot{q}_{\text{v}}$ is to improve the cell aC and α_{rev}. This will increase the number of ions that can be stored in each electrode and the heat released or absorbed for each mole of ions separated. Faster charging/discharging will also increase system capacity by reducing the cycling time, but it will also increase irreversible ohmic heat generation. Hence, it is important to operate the system utilizing cells with lower ohmic losses and larger reversible heat. For example, $\dot{q}_{\text{v}}$ can be doubled (30 kW m^{-3}) when the cell is operated at two-fold increase in charging/discharging rates (16.6 A m^{-2}) with the half-reduced cell ohmic resistance (6.5 Ω).

Similar to other caloric heat pumping devices, COP would drop in cascaded

cells when heat losses are significant [20]. By arranging the cells in a cascade manner, the projected adiabatic temperature span can reach up to 30 °C, corresponding to a COP of 3. When U $>$ 5 W m^{-2} $°C^{-1}$, the temperature span of the cascaded system would decrease significantly by 2 °C, resulting in a COP of 1. Hence, it is important to design a housing that thermally seals the cascaded cells and reduces the dead thermal mass.

For the scaled-up systems, the performance estimates with liquid pumps and controllers involved in the cyclic contact processes will have to be addressed in details. The size of hot and cold side heat exchangers in each secondary loop is important for achieving the high efficiency of heat exchange between the cascade cells and secondary hydronic loop. Real-world building operation involves dynamic loads. Future works could involve simulating impacts of TCHP control strategies with system dynamics and optimizing for external conditions such as temperature forecast, electricity price, and end grid carbon intensity. Understanding how those factors impact the system performance will be important to consider for practical applications at scale.

Figure 7(B) shows the performance comparison of heat pumping and energy storage of the TCHP and air-source heat pump (ASHP) with thermal energy storage (TES) systems. Multifunctional packaged ASHP integrated with phase change materials (PCM) for combined heating and TES in buildings have received increasing interest among researchers [79]. The technologies used for the performance comparisons were R410A ASHP and paraffin wax PCM [74, 75], R32 ASHP and paraffin PCM [77], R134a/R410A ASHP water and paraffin mixture PCM [72], and general HP geometries and PCM properties that were used for numerical simulations [73, 76].

For reasonable comparisons, the $\dot{q}_v$s for the ASHP and PCM systems were obtained from the reported discharge power density, and the chamber volumes were obtained from TES storage tank sizes including the volume of the PCM materials. The data shown are typical values based on criteria: (i) the systems consisting of both heat pump and PCM with supporting components, (ii) measurement taken from both thermal energy storage (in kWh) and $\dot{q}_v$ on the same systems, (iii) TES storage tank volumes explicitly reported, and (iv) the data reported within 10 years. Moreover, the amount of energy stored was normalized with the TES storage tank volumes to determine the range of ED. This is because the reported energy density of a device can be varied on the same systems based on the applied currents or

fluid mass flow rates [80].

Although achieving comparable $\Delta T_{\text{span,max}}$ for TCHPs relative to commercially available heat pump systems is still challenging, thermocapacitive effects have a significant potential regarding heating power density. The thermocapacitive cells store electrical energy electrostatically, which allows for very rapid charging and discharging. The current generated when draining the cell can just be used to provide heating. This is fundamentally different from the ASHP with TES systems, where the heating power is limited by the mass flow rate and thermal conductivity of PCM materials [81]. One of the potential applications for the TCHPs could be a combination heat pump system in residential buildings, that requires the large and rapid transitions of refrigerant temperatures and heating capacity due to the combined space and water heating loads [82].

Table 3 summarizes the comparison of TCHP to VC system combined with energy storage. A methodology and data for predicting the economics of TCHPs and VCs were adapted from James et al. [20]. The unit was assumed to have a heating capacity of 1 kW and to have the capability to provide heating and energy storage. The cost of supercapacitors could be as low as 8 \$ kW^{-1} of electrical power [83]. Using the measured COP of 2 to convert to thermal power, an estimated cost is 4 \$ $\text{kW}_{\text{heating}}^{-1}$ of heating (i.e., 8 \$ kW^{-1}/COP). The energy storage capacity can be estimated based on the heating cost (in \$ $\text{kW}_{\text{heating}}^{-1}$) and the energy cost of supercapacitor of 2,500 \$ kWh^{-1}. For example, a 1 kW TCHP would have a storage capacity of 1.6 Wh (4 \$ $\text{kW}_{\text{heating}}^{-1} \times 1$ $\text{kW}_{\text{heating}}$/2,500 \$ kWh^{-1}).

TCC cooling and heating are driven by supercapacitiors, and VC cooling and heating are driven by mechanical compressors. For direct cost comparison, the cost of a VC compressor was used instead of using all costs of the VC components. The heating cost of the VC compressor of 90 \$ $\text{kW}_{\text{heating}}^{-1}$ was combined with the costs of energy storage materials including PCM (3 \$ kWh^{-1}) and lithium ion battery (215 \$ kWh^{-1}) [84, 85]. The results show that a VC system having 1 kW of heating and 1.6 Wh of energy storage would have nearly 90 \$ $\text{kW}_{\text{heating}}^{-1}$. The heating cost of the compressor accounts for nearly 99% of the total costs of the VC systems when the energy storage capacity is small. This means that the heating costs of TCHPs could be less than those of VCs for small-scale heat pumping applications.

Although the projected performance of solid-regenerated TCHPs is higher

Table 3: Comparison of TCHP to VC system combined with energy storage. The data of solid-regenerated TCHP were obtained based on this study. The data of liquid-regenerated TCHP, VC compressor + TES, and VC compressor + BES were adapted from James et al. [20].

Reference	ΔT_{span} (°C)	$\dot{q}_{\text{v}}$ (kW m^{-3})	COP/COP$_{\text{Carnot}}$ (-)	Cost ($ kW$^{-1}_{\text{heating}}$)
(e,t)Solid-Regenerated TCHP	12	15	0.08	4
(t)Solid-Regenerated TCHP	30	16	0.32	4
(E)Liquid-Regenerated TCHP	0.24	0.58[a]	0.0004	29.6
(t)VC Compressor + TES	∼60[b]	142.5[c]	0.22	90
(t)VC Compressor + BES	∼60[b]	142.5[c]	0.22	90.3

Cost based on a system capable of providing 1 kW of heating and 11.8 Wh of energy storage.

(t)Theoretical predictions; (e,t)Testing components; (E)Testing full cycles.

[a]Based on total cell volume in James et al. [20].

[b]Based on single-stage cycles in Chakravarthy et al. [86].

[c]Based on R410A in El Fil et al. [6].

than that of a liquid-regenerated system, substantial work is still needed to compete with conventional technologies. Enhancing $\Delta T_{\text{span,max}}$ for the TCHPs requires (i) the optimization of the electrode microstructure and composition to increase ion storage capacity and incorporate redox reactions into the charge storage process [52], (ii) increase in the thermopower of enclosed electrochemical cells by changing solvation entropy [50, 87, 88], and (iii) optimization of system architectures to maximize heat transfers and internal heat recuperation for high-efficiency hybrid TCHP and storage. Given the fact that the comparisons are based on the ED$_{\text{max}}$ of the TCHPs that are an order of magnitude lower than that of the ASHP and PCM energy storage technologies, there are significant potential remains to improve the performance of the TCHPs.

Increasing either the electrolyte wetting or the specific surface area of the materials could lead to a higher-performing product. This is because the higher number of ions that can be stored in electrodes produces larger capacitances and entropy changes. The use of electrocapillary effects [89], the control of the particle size ratio of the electrodes [90], and the proper choice of electrolyte-electrode pairing [16] will influence the degree of electrolyte filling and wetting for thick and pressed electrodes. The larger specific surface area can be achieved using electroplating [91], nanostructuring [92], and additive

manufacturing [93]. Breakthroughs in both materials and cell designs would allow thermocapacitive cells to enable usable heat pumping devices.

A distinctive characteristic of TCHP systems is to integrate energy storage processes with heating and cooling components. Such hybridization strategies are fundamentally different from most emerging heat pumping equipment [5, 6] which are mostly single-function thermal devices for moving or transferring heat. By making use of multifunctional devices, the future cooling and heating systems may provide increased utility and load flexibility [94]. This could be beneficial to advanced building cooling and heating and other thermal management applications as energy storage becomes increasingly important for energy system integration.

5. Conclusion

A major contribution of this paper is to investigate thermocapacitive cell designs that enable larger adiabatic temperature spans for heat pumping applications. To this end, pouch type cells were prototyped and modeled, and tested using a micro-calorimeter. The cell-level experimental results were combined with the TCHP cycle model to evaluate the influence of multiple cells on the overall temperature span. The following bullet items summarize the conclusion of this study based on calorimetry and simulation results.

- The activated carbon based cells (24.08 cm^2) with 1 M LiCl aqueous electrolyte produce higher reversible heat and capacitance than those with other mixed solvent electrolytes. The cells have the averaged pore size of 1.5 µm, low Bi of 0.01, and high $D_{\text{th,eff}}$ of 0.145 $cm^2\ s^{-1}$. Based on the low Bi and $D_{\text{th,eff}}$ of the cells, the lumped-element model and quasi-steady state approximation can be used to predict the cell temperature.
- The measured $\dot{q}_{\text{T,rev}}$s are symmetric exothermic and endothermic processes. The heat energy produced during charging and discharging cycles is recovered when the process is reversed. The peak reversible $\dot{q}_{\text{T,rev}}$ decreases from 3.8 W m^{-2} to 1.6 W m^{-2} at higher currents due to the reduced capacitance from 5.8 F to 3.5 F. This corresponds to the decrease in the averaged α_{rev} from -1.7 mV $°C^{-1}$ to -0.65 mV $°C^{-1}$. The faster charging and discharging leave more unused area and en-

ergy in the capacitive devices, decreasing the electrolyte Δs from 45.5 J kg^{-1} °C^{-1} to 1.7 J kg^{-1} °C^{-1} and thus reduced $\dot{q}_{\mathrm{T,rev}}$ and α_{rev}.

- The change in LiCl cell temperature is strongly affected by U values. When U is 1 W m^{-2} °C^{-1}, ΔT_{span} is 0.9°-2.7 °C. When U is 5 W m^{-2} °C^{-1}, ΔT_{span} is 0.57 °C to 0.22 °C. Those ΔT_{span} are less than 0.03 °C when U is 100 W m^{-2} °C^{-1}. The decrease in ΔT_{span} at higher U is a result of larger heat losses to the ambient. The maximum temperature span of 2.7 °C at the U of 1 W m^{-2} °C^{-1} of the LiCl cells is higher than that of other reported cells designed less than 100 F.

- The faster charging and discharging increase the ratio of Joule heating to total heating from 58% to 96.5%. To reduce the Joule heating and improve the ΔT_{span} of the cells, it is important to reduce the cell ohmic resistance. Moreover, the cell provides a potential ΔT_{span} increase of over 50% by reducing mc_{p} and improving α_{rev} by 50%, respectively. This can be achieved by fabricating thinner electrodes [57], oxides electrodes that involves Faradaic reactions [52], binary solvent and anion engineering [50], and organic electrolytes having 2 times lower density.

- By arranging the nine prototyped LiCl cells in a cascade manner, the TCHPs have a potential to produce comparable ΔT_{span} to other electrochemical and caloric heat pumping technologies. The maximum ΔT_{span} is 12 °C at the U of 1 W m^{-2} °C^{-1}, and the $\dot{q}_{\mathrm{v}}$ is 15 kW m^{-3}. This $\Delta T_{\mathrm{span,max}}$ is comparable to that of electrocaloric devices based on multilayer capacitors [61, 62]. If the C and α_{rev} of the cells were doubled, the $\mathrm{COP_{max}}/\mathrm{COP_{Carnot}}$ could reach up to 0.33. The projected performance supersedes those of the other caloric and electrochemical heat pumps.

- Although achieving comparable $\Delta T_{\mathrm{span,max}}$ for TCHPs relative to commercially available heat pump systems is still challenging, the thermocapacitive effects have a significant potential regarding heating power density. This is because the TCHPs store electrical energy electrostatically, which allows for very rapid charging and discharging as well as delivering heat. One of the potential applications for the TCHPs could be a combination heat pump system in residential buildings, which requires the large and rapid transitions of refrigerant temperatures and heating capacity [82].

- The TCHPs could be beneficial to the development of advanced building cooling and heating systems as energy storage becomes increasingly important for energy system integration. To advance the TCHP technologies, the recommended future research directions are (i) the optimization of the electrode microstructure and composition to increase ion storage capacity and incorporate redox reactions into the charge storage process [52], (ii) increase in the thermopower of enclosed electrochemical cells by changing solvation entropy [50, 87, 88], and (iii) optimization of system architectures to maximize heat transfers and internal heat recuperation for high-efficiency hybrid TCHP and energy storage.

6. Acknowledgment

This research was supported by Kumoh National Institute of Technology (2025∼2027). This work was authored by the National Renewable Energy Laboratory (NREL) for the U.S. Department of Energy (DOE) under Contract No. DE-AC36-08GO28308. This work was supported by the Laboratory Directed Research and Development (LDRD) Program at NREL. The views expressed in the article do not necessarily represent the views of the DOE or the U.S. Government. The U.S. Government retains and the publisher, by accepting the article for publication, acknowledges that the U.S. Government retains a nonexclusive, paid-up, irrevocable, worldwide license to publish or reproduce the published form of this work, or allow others to do so, for U.S. Government purposes. The authors also thank Joshua Major, Dr. Adawale Odukomaiya, and Dr. Kerry Rippy for helpful discussions.

7. Author Contributions

Conceptualization, J.K., N.J.; Methodology, J.K., B.O., N.J.; Formal Analysis, J.K., B.O.; Software, J.K., N.J.; Investigation, J.K., B.O.; Data Curation, J.K.; Writing - Original Draft, J.K.; Writing - Review & Editing, J.K., N.J., B.O., D.F.; Supervision, J.K., N.J.; Project Administration, J.K., N.J.; Funding Acquisition, J.K., N.J., D.F.

References

[1] U.S. Energy Information Agency. (2025). Mnothly energy review. https://www.eia.gov/totalenergy/data/monthly/

[2] IEA. (2018). The future of cooling. *IEA, Paris*. https://www.iea.org/reports/the-future-of-cooling

[3] IEA. (2022). The future of heat pumps. *IEA, Paris*. https://www.iea.org/reports/the-future-of-heat-pumps

[4] McLinden, M. O., Seeton, C. J., & Pearson, A. (2020). New refrigerants and system configurations for vapor-compression refrigeration. *Science*, *370*(6518), 791–796. https://doi.org/10.1126/science.abe3692

[5] Goetzler, W., Zogg, R., Young, J., & Johnson, C. (2014). Alternatives to vapor-compression HVAC technology. *ASHRAE Journal*, *56*, 12–23.

[6] El Fil, B., Boman, D. B., Tambasco, M. J., & Garimella, S. (2021). A comparative assessment of space-conditioning technologies. *Applied Thermal Engineering*, *182*, 116105. https://doi.org/10.1016/j.applthermaleng.2020.116105

[7] Cui, S., Odukomaiya, A., & Vidal, J. (2021). Materials research and development needs to enable efficient and electrified buildings. *MRS Bulletin*, *46*. https://doi.org/10.1557/s43577-021-00241-x

[8] Sukma, M. S., Zheng, Y., & Scott, S. A. (2024). Dicalcium ferrite: A chemical heat pump in integrated carbon capture and chemical looping combustion for the steel industry. *Chemical Engineering Journal*, *488*, 150658. https://doi.org/10.1016/j.cej.2024.150658

[9] Šulgan, B., Furda, P., & Labovská, Z. (2023). Economic and environmental assessment of heat pump integration in thermally coupled hybrid separation. *Chemical Engineering Journal*, *471*, 144298. https://doi.org/10.1016/j.cej.2023.144298

[10] Li, Q., Hao, Y., & Sun, L. (2025). Modeling and evaluation of a steam and power cogeneration system of proton exchange membrane fuel cell coupled high temperature heat pump. *Chemical Engineering Journal*, *505*, 159432. https://doi.org/10.1016/j.cej.2025.159432

[11] Lin, J., Zhang, Z., Zhu, X., Meng, C., Li, N., Chen, J., & Zhao, Y. (2019). Performance evaluation and parametric optimization strategy of a thermocapacitive heat engine to harvest low-grade heat. *Energy Conversion and Management*, *184*, 40–47. https://doi.org/10.1016/j.enconman.2019.01.012

[12] Janssen, M., & van Roij, R. (2017). Reversible heating in electric double layer capacitors. *Phys. Rev. Lett.*, *118*, 096001. https://doi.org/10.1103/PhysRevLett.118.096001

[13] Kitanovski, A., Plaznik, U., Tomc, U., & Poredoš, A. (2015). Present and future caloric refrigeration and heat-pump technologies. *Interna-*

tional Journal of Refrigeration, *57*, 288–298. https://doi.org/10.1016/j.ijrefrig.2015.06.008

[14] Kundu, A., & Fisher, T. S. (2018). Harnessing the thermogalvanic effect of the ferro/ferricyanide redox couple in a thermally chargeable supercapacitor. *Electrochimica Acta*, *281*, 357–369. https://doi.org/10.1016/j.electacta.2018.05.164

[15] Buckingham, M. A., Zhang, S., Liu, Y., Chen, J., Marken, F., & Aldous, L. (2021). Thermogalvanic and thermocapacitive behavior of superabsorbent hydrogels for combined low-temperature thermal energy conversion and harvesting. *ACS Applied Energy Materials*, *4*(10), 11204–11214. https://doi.org/10.1021/acsaem.1c02060

[16] Zhao, L., Li, Y., Yu, M., Peng, Y., & Ran, F. (2023). Electrolyte-wettability issues and challenges of electrode materials in electrochemical energy storage, energy conversion, and beyond. *Advanced Science*, *10*(17), 2300283. https://doi.org/10.1002/advs.202300283

[17] Lao, Y., Tang, P., Zeng, J., Xu, S., Zhu, J., Dou, Q., Xiao, X., & Yan, X. (2025). Revealing the limitations of the thermocapacitive cycle [PMID: 39814007]. *ACS Nano*, *19*(3), 3895–3905. https://doi.org/10.1021/acsnano.4c16370

[18] Duan, J., Yu, B., Huang, L., Hu, B., Xu, M., Feng, G., & Zhou, J. (2021). Liquid-state thermocells: Opportunities and challenges for low-grade heat harvesting. *Joule*, *5*(4), 768–779. https://doi.org/10.1016/j.joule.2021.02.009

[19] Qian, X., Ma, Z., Huang, Q., Jiang, H., & Yang, R. (2024). Thermodynamics of ionic thermoelectrics for low-grade heat harvesting. *ACS Energy Letters*, *9*(2), 679–706. https://doi.org/10.1021/acsenergylett.3c02448

[20] James, N., Kim, J., Özdoğru, B., & Finegan, D. P. (2025). Dual-functional thermocapacitive heat pump with electrochemical supercapacitors for building thermal management and energy storage. *Device*, 100895. https://doi.org/10.1016/j.device.2025.100895

[21] Rani, J. R., Thangavel, R., Oh, S.-I., Lee, Y. S., & Jang, J.-H. (2019). An ultra-high-energy density supercapacitor; fabrication based on thiol-functionalized graphene oxide scrolls. *Nanomaterials*, *9*(2). https://doi.org/10.3390/nano9020148

[22] Li, Z., Gadipelli, S., Li, H., Howard, C. A., Brett, D. J. L., Shearing, P. R., Guo, Z., Parkin, I. P., & Li, F. (2020). Tuning the interlayer spacing of graphene laminate films for efficient pore utilization towards

compact capacitive energy storage. *Nature Energy*, *5*, 160–168. https://doi.org/10.1038/s41560-020-0560-6

[23] Simon, P., & Gogotsi, Y. (2020). Perspectives for electrochemical capacitors and related devices. *Nature Energy*, *19*, 1151–1163. https://doi.org/10.1038/s41563-020-0747-z

[24] Odukomaiya, A., Woods, J., James, N., Kaur, S., Gluesenkamp, K. R., Kumar, N., Mumme, S., Jackson, R., & Prasher, R. (2021). Addressing energy storage needs at lower cost via on-site thermal energy storage in buildings. *Energy Environ. Sci.*, *14*, 5315–5329. https://doi.org/10.1039/D1EE01992A

[25] Bard, A., & Faulkner, L. (2001). Electrochemical methods: Fundamentals and applications. *John Wiley Sons, New York, NY*. https://www.energy.gov/eere/fuelcells/downloads/manufacturing-cost-analysis-100-and-250-kw-fuel-cell-systems-primary-power

[26] Hess, T., Maier, L., Corhan, P., Schäfer–Welsen, O., Wöllenstein, J., & Bartholomé, K. (2019). Modelling cascaded caloric refrigeration systems that are based on thermal diodes or switches. *International Journal of Refrigeration*, *103*, 215–222. https://doi.org/10.1016/j.ijrefrig.2019.04.013

[27] Wang, Y., Zhang, Z., Usui, T., Benedict, M., Hirose, S., Lee, J., Kalb, J., & Schwartz, D. (2020). A high-performance solid-state electrocaloric cooling system. *Science*, *370*(6512), 129–133. https://doi.org/10.1126/science.aba2648

[28] Härtel, A., Janssen, M., Weingarth, D., Presser, V., & van Roij, R. (2015). Heat-to-current conversion of low-grade heat from a thermocapacitive cycle by supercapacitors. *Energy Environ. Sci.*, *8*, 2396–2401. https://doi.org/10.1039/C5EE01192B

[29] Tester, J. W., & Modell, M. (1997). *Thermodynamics and its Applications-3rd Edition*. Pearson College Div.

[30] Dandeville, Y. (2012). Analyse thermique et électrochimique de supercondensateurs carbone-MnO2 en milieu aqueux. *PhD Thesis, Université de Nantes, Français*. https://tel.archives-ouvertes.fr/tel-00765136

[31] Fink, K. E., Polzin, B. J., Vaughey, J. T., Major, J. J., Dunlop, A. R., Trask, S. E., Jeka, G. T., Spangenberger, J. S., & Keyser, M. A. (2022). Influence of metallic contaminants on the electrochemical and thermal behavior of Li-ion electrodes. *Journal of Power Sources*, *518*, 230760. https://doi.org/10.1016/j.jpowsour.2021.230760

[32] Hansen, L. D., Transtrum, M. K., Quinn, C., & Demarse, N. (2016). Enzyme-catalyzed and binding reaction kinetics determined by titration calorimetry [Microcalorimetry in the BioSciences - Principles and Applications]. *Biochimica et Biophysica Acta (BBA) - General Subjects*, *1860*(5), 957–966. https://doi.org/10.1016/j.bbagen.2015.12.018

[33] Taylor, B., & Kuyatt, C. (1994). Guidelines for evaluating and expressing the uncertainty of nist measurement results 1994 edition. https://doi.org/10.6028/NIST.tn.1297

[34] Munteshari, O., Lau, J., Krishnan, A., Dunn, B., & Pilon, L. (2018). Isothermal calorimeter for measurements of time-dependent heat generation rate in individual supercapacitor electrodes. *Journal of Power Sources*, *374*, 257–268. https://doi.org/10.1016/j.jpowsour.2017.11.012

[35] Munteshari, O., Lau, J., Ashby, D. S., Dunn, B., & Pilon, L. (2018). Effects of constituent materials on heat generation in individual EDLC electrodes. *Journal of The Electrochemical Society*, *165*(7), A1547. https://doi.org/10.1149/2.0771807jes

[36] Likitchatchawankun, A., Whang, G., Lau, J., Munteshari, O., Dunn, B., & Pilon, L. (2020). Effect of temperature on irreversible and reversible heat generation rates in ionic liquid-based electric double layer capacitors. *Electrochimica Acta*, *338*, 135802. https://doi.org/10.1016/j.electacta.2020.135802

[37] Helseth, L. (2021). Comparison of methods for finding the capacitance of a supercapacitor. *Journal of Energy Storage*, *35*, 102304. https://doi.org/10.1016/j.est.2021.102304

[38] Comet Technologies Canada Inc. (2022). Dragonfly 2022.2 [Computer software]. Retrieved January 23, 2025, from https://www.theobjects.com/dragonfly

[39] Cooper, S., Bertei, A., Shearing, P., Kilner, J., & Brandon, N. (2016). Taufactor: An open-source application for calculating tortuosity factors from tomographic data. *SoftwareX*, *5*, 203–210. https://doi.org/10.1016/j.softx.2016.09.002

[40] Bell, I. H., Wronski, J., Quoilin, S., & Lemort, V. (2014). Pure and pseudo-pure fluid thermophysical property evaluation and the open-source thermophysical property library CoolProp. *Industrial & Engineering Chemistry Research*, *53*(6), 2498–2508. https://doi.org/10.1021/ie4033999

[41] Lemmon, E. W., Bell, I. H., Huber, M. L., & McLinden, M. O. (2018). NIST Standard Reference Database 23: Reference Fluid Thermody-

namic and Transport Properties-REFPROP, Version 10.0, National Institute of Standards and Technology. https://doi.org/10.18434/T4/1502528

[42] Jia, Y., Zhang, H., & Zhang, J. (2022). The effect of peroxide cross-linking on the thermal conductivity and crystallinity of low-density polyethylene. *Materials Today Communications*, *31*, 103735. https://doi.org/10.1016/j.mtcomm.2022.103735

[43] COMSOL Multiphysics v. 6.2. (2023). COMSOL AB, Stockholm, Sweden. https://www.comsol.com

[44] Verbrugge, M. W., & Liu, P. (2005). Microstructural analysis and mathematical modeling of electric double-layer supercapacitors. *Journal of The Electrochemical Society*, *152*(5), D79. https://doi.org/10.1149/1.1878052

[45] Gogotsi, Y., & Penner, R. M. (2018). Energy storage in nanomaterials – capacitive, pseudocapacitive, or battery-like? [PMID: 29580061]. *ACS Nano*, *12*(3), 2081–2083. https://doi.org/10.1021/acsnano.8b01914

[46] Python. (2023). Python language reference, version 3.11.2. *Python Software Foundation*. Retrieved November 10, 2023, from https://www.python.org/

[47] Incorpera, F., DeWitt, D., Bergman, T., & Lavine, A. (2006). *Fundamentals of Heat and Mass Transfer-6th Edition*. John Wiley.

[48] Burheim, O. S., Aslan, M., Atchison, J. S., & Presser, V. (2014). Thermal conductivity and temperature profiles in carbon electrodes for supercapacitors. *Journal of Power Sources*, *246*, 160–166. https://doi.org/10.1016/j.jpowsour.2013.06.164

[49] Zhang, Y., Liu, Z., Sun, X., An, Y., Zhang, X., Wang, K., Dong, C., Huo, Q., Wei, T., & Ma, Y. (2019). Experimental study of thermal charge–discharge behaviors of pouch lithium-ion capacitors. *Journal of Energy Storage*, *25*, 100902. https://doi.org/10.1016/j.est.2019.100902

[50] Zeng, Y., Yu, B., Chen, M., Zhang, J., Liu, P., Guo, J., Wang, J., Feng, G., Zhou, J., & Duan, J. (2025). Solvation entropy engineering of thermogalvanic electrolytes for efficient electrochemical refrigeration. *Joule*, *9*, 101822. https://doi.org/10.1016/j.joule.2025.101822

[51] Schiffer, J., Linzen, D., & Sauer, D. U. (2006). Heat generation in double layer capacitors. *Journal of Power Sources*, *160*(1), 765–772. https://doi.org/10.1016/j.jpowsour.2005.12.070

[52] Dandeville, Y., Guillemet, P., Scudeller, Y., Crosnier, O., Athouel, L., & Brousse, T. (2011). Measuring time-dependent heat profiles of aque-

ous electrochemical capacitors under cycling. *Thermochimica Acta*, *526*(1), 1–8. https://doi.org/10.1016/j.tca.2011.07.027

[53] Gualous, H., Louahlia, H., & Gallay, R. (2011). Supercapacitor characterization and thermal modelling with reversible and irreversible heat effect. *IEEE Transactions on Power Electronics*, *26*(11), 3402–3409. https://doi.org/10.1109/TPEL.2011.2145422

[54] Zhang, X., Wang, W., Lu, J., Hua, L., & Heng, J. (2016). Reversible heat of electric double-layer capacitors during galvanostatic charging and discharging cycles. *Thermochimica Acta*, *636*, 1–10. https://doi.org/10.1016/j.tca.2016.04.014

[55] Parvini, Y., Siegel, J. B., Stefanopoulou, A. G., & Vahidi, A. (2016). Supercapacitor electrical and thermal modeling, identification, and validation for a wide range of temperature and power applications. *IEEE Transactions on Industrial Electronics*, *63*(3), 1574–1585. https://doi.org/10.1109/TIE.2015.2494868

[56] Park, Y., Kim, J., Kim, C., Lee, S.-M., Kang, C., & Seol, J. H. (2022). In situ and operando thermal characterization in aqueous electric double layer capacitors using the 3 hot-wire method. *International Journal of Heat and Mass Transfer*, *188*, 122632. https://doi.org/10.1016/j.ijheatmasstransfer.2022.122632

[57] Liu, T., Wang, K., Chen, Y., Zhao, S., & Han, Y. (2019). Dominant role of wettability in improving the specific capacitance [Special Issue: Ionic Liquids in Energy and Environment]. *Green Energy Environment*, *4*(2), 171–179. https://doi.org/10.1016/j.gee.2019.01.010

[58] Lilley, D., & Prasher, R. (2022). Ionocaloric refrigeration cycle. *Science*, *378*(6626), 1344–1348. https://doi.org/10.1126/science.ade1696

[59] Rajan, A., McKay, I. S., & Yee, S. K. (2022). Continuous electrochemical refrigeration based on the Brayton cycle. *Nature Energy*. https://doi.org/10.1038/s41560-021-00975-7

[60] Ma, R., Zhang, Z., Tong, K., Huber, D., Kornbluh, R., Ju, Y. S., & Pei, Q. (2017). Highly efficient electrocaloric cooling with electrostatic actuation. *Science*, *357*(6356), 1130–1134. https://doi.org/10.1126/science.aan5980

[61] Plaznik, U., Vrabelj, M., Kutnjak, Z., Malič, B., Rožič, B., Poredoš, A., & Kitanovski, A. (2019). Numerical modelling and experimental validation of a regenerative electrocaloric cooler. *International Journal of Refrigeration*, *98*, 139–149. https://doi.org/10.1016/j.ijrefrig.2018.10.029

[62] Torelló, A., Lheritier, P., Usui, T., Nouchokgwe, Y., Gérard, M., Bouton, O., Hirose, S., & Defay, E. (2020). Giant temperature span in electrocaloric regenerator. *Science*, *370*(6512), 125–129. https://doi.org/10.1126/science.abb8045

[63] Li, J., Torelló, A., Kovacova, V., Prah, U., Aravindhan, A., Granzow, T., Usui, T., Hirose, S., & Defay, E. (2023). High cooling performance in a double-loop electrocaloric heat pump. *Science*, *382*(6672), 801–805. https://doi.org/10.1126/science.adi5477

[64] Jacobs, S., Auringer, J., Boeder, A., Chell, J., Komorowski, L., Leonard, J., Russek, S., & Zimm, C. (2014). The performance of a large-scale rotary magnetic refrigerator [New Developments in Magnetic Refrigeration]. *International Journal of Refrigeration*, *37*, 84–91. https://doi.org/10.1016/j.ijrefrig.2013.09.025

[65] Choi, J., Lee, S., & Kim, M. S. (2022). A testbed for a magnetic refrigeration system at room temperature and its experimental evaluation. *Energy Conversion and Management*, *265*, 115771. https://doi.org/10.1016/j.enconman.2022.115771

[66] Lin, Y., Wang, J., Dai, W., Qiao, K., Zhou, H., Zhao, T., Hu, F., & Shen, B. (2024). A full solid-state conceptual magnetocaloric refrigerator based on hybrid regeneration. *The Innovation*, *5*(4), 100645. https://doi.org/10.1016/j.xinn.2024.100645

[67] Ahčin, Ž., Dall'Olio, S., Žerovnik, A., Baškovič, U. Ž., Porenta, L., Kabirifar, P., Cerar, J., Zupan, S., Brojan, M., Klemenc, J., & Tušek, J. (2022). High-performance cooling and heat pumping based on fatigue-resistant elastocaloric effect in compression. *Joule*, *6*(10), 2338–2357. https://doi.org/10.1016/j.joule.2022.08.011

[68] Qian, S., Catalini, D., Muehlbauer, J., Liu, B., Mevada, H., Hou, H., Hwang, Y., Radermacher, R., & Takeuchi, I. (2023). High-performance multimode elastocaloric cooling system. *Science*, *380*(6646), 722–727. https://doi.org/10.1126/science.adg7043

[69] Atta, R. M. (2017). Solar thermoelectric cooling using closed loop heat exchangers with macrochannels. *Heat Mass Transfer*, *53*, 2241–2254. https://doi.org/10.1007/s00231-017-1965-z

[70] Kim, J., Mishra, A., Braun, J. E., Groll, E. A., Rodríguez-López, J., & Ziviani, D. (2023). Electrochemically driven phase transformation for high-efficiency heat pumping. *Cell Reports Physical Science*, *4*(4), 101369. https://doi.org/10.1016/j.xcrp.2023.101369

[71] Klinar, K., Law, J. Y., Franco, V., Moya, X., & Kitanovski, A. (2024). Perspectives and energy applications of magnetocaloric, pyromagnetic, electrocaloric, and pyroelectric materials. *Advanced Energy Materials*, *14*(39), 2401739. https://doi.org/10.1002/aenm.202401739

[72] Zou, D., Ma, X., Liu, X., Zheng, P., Cai, B., Huang, J., Guo, J., & Liu, M. (2017). Experimental research of an air-source heat pump water heater using water-pcm for heat storage. *Applied Energy*, *206*, 784–792. https://doi.org/10.1016/j.apenergy.2017.08.209

[73] Xu, T., Humire, E. N., Chiu, J. N., & Sawalha, S. (2021). Latent heat storage integration into heat pump based heating systems for energy-efficient load shifting. *Energy Conversion and Management*, *236*, 114042. https://doi.org/10.1016/j.enconman.2021.114042

[74] Yu, M., Zhang, C., Fan, Y., Zhang, X., & Zhao, Y. (2021). Performance study of phase change charging/discharging processes of condensing heat storage in cold regions based on a mathematical model. *Applied Thermal Engineering*, *182*, 115805. https://doi.org/10.1016/j.applthermaleng.2020.115805

[75] Lin, Y., Fan, Y., Yu, M., Jiang, L., & Zhang, X. (2022). Performance investigation on an air source heat pump system with latent heat thermal energy storage. *Energy*, *239*, 121898. https://doi.org/10.1016/j.energy.2021.121898

[76] Inkeri, E., Tynjälä, T., & Nikku, M. (2022). Numerical modeling of latent heat thermal energy storage integrated with heat pump for domestic hot water production. *Applied Thermal Engineering*, *214*, 118819. https://doi.org/10.1016/j.applthermaleng.2022.118819

[77] Emhofer, J., Marx, K., Sporr, A., Barz, T., Nitsch, B., Wiesflecker, M., & Pink, W. (2022). Experimental demonstration of an air-source heat pump application using an integrated phase change material storage as a desuperheater for domestic hot water generation. *Applied Energy*, *305*, 117890. https://doi.org/10.1016/j.apenergy.2021.117890

[78] Ahčin, Ž., Liang, J., Engelbrecht, K., & Tušek, J. (2021). Thermo-hydraulic evaluation of oscillating-flow shell-and-tube-like regenerators for (elasto)caloric cooling. *Applied Thermal Engineering*, *190*, 116842. https://doi.org/10.1016/j.applthermaleng.2021.116842

[79] Hu, Y., & Shen, B. (2025). Development and evaluation of a multi-functional heat pump with embedded thermal storage. *Applied Thermal Engineering*, *267*, 125862. https://doi.org/10.1016/j.applthermaleng.2025.125862

[80] Woods, J., Mahvi, A., Goyal, A., Kozubal, E., Odukomaiya, A., & Jackson, R. (2021). Rate capability and ragone plots for phase change thermal energy storage. *Nat Energy*, *6*, 295–302. https://doi.org/10.1038/s41560-021-00778-w

[81] Shamberger, P. J. (2021). Mapping design trade-offs. *Nature Energy*, *6*, 221–222. https://doi.org/10.1038/s41560-021-00803-y

[82] Kim, J., James, N., & Maguire, J. (2024). Investigation of a high-temperature combination heat pump for lower-cost electrification in multifamily buildings. *Applied Energy*, *376*, 124225. https://doi.org/10.1016/j.apenergy.2024.124225

[83] Dutta, A., Mitra, S., Basak, M., & Banerjee, T. (2023). A comprehensive review on batteries and supercapacitors: Development and challenges since their inception. *Energy Storage*, *5*(1), e339. https://doi.org/https://doi.org/10.1002/est2.339

[84] Hirschey, J. R., Kumar, N., Turnaoglu, T., Gluesenkamp, K. R., & Graham, S. (2021). Review of low-cost organic and inorganic phase change materials with phase change temperature between 0 C and 65 C. *International High Performance Building Conference. West Lafayette, Purdue University*. https://docs.lib.purdue.edu/ihpbc/389

[85] Ramasamy, V., Zuboy, J., Woodhouse, M., O'Shaughnessy, E., Feldman, D., Desai, J., Walker, A., Margolis, R., & Basore, P. (2023). U.S. solar photovoltic system and energy storage cost benchmarks, with minimum sustainable price analysis: Q1 2023. *Golden, CO: National Renewable Energy Laboratory. NREL/TP-7A40-87303.* https://www.nrel.gov/docs/fy23osti/87303.pdf

[86] Chakravarthy, V. S., Shah, R. K., & Venkatarathnam, G. (2011). A review of refrigeration methods in the temperature range 4–300 K. *Journal of Thermal Science and Engineering Applications*, *3*(2), 020801. https://doi.org/10.1115/1.4003701

[87] Chen, Y., Huang, Q., Liu, T.-H., Qian, X., & Yang, R. (2023). Effect of solvation shell structure on thermopower of liquid redox pairs. *EcoMat*, *5*(9), e12385. https://doi.org/10.1002/eom2.12385

[88] Kim, T., Lee, J. S., Lee, G., Yoon, H., Yoon, J., Kang, T. J., & Kim, Y. H. (2017). High thermopower of ferri/ferrocyanide redox couple in organic-water solutions. *Nano Energy*, *31*, 160–167. https://doi.org/10.1016/j.nanoen.2016.11.014

[89] Cui, H., Song, Y., Ren, D., Wang, L., & He, X. (2024). Electrocapillary boosting electrode wetting for high-energy lithium-ion batteries. *Joule*, *8*(1), 29–44. https://doi.org/10.1016/j.joule.2023.11.012

[90] Jeon, D. H. (2021). Enhancing electrode wettability in lithium-ion battery via particle-size ratio control. *Applied Materials Today*, *22*, 100976. https://doi.org/10.1016/j.apmt.2021.100976

[91] Lim, A., Kim, J., Lee, H. J., Kim, H.-J., Yoo, S. J., Jang, J. H., Young Park, H., Sung, Y.-E., & Park, H. S. (2020). Low-loading IrO2 supported on Pt for catalysis of PEM water electrolysis and regenerative fuel cells. *Applied Catalysis B: Environmental*, *272*, 118955. https://doi.org/10.1016/j.apcatb.2020.118955

[92] Cao, B., He, X., Sorge, J. B., Lalany, A., Ahadi, K., Afshar, A., Olsen, B. C., Hauger, T. C., Mobarok, M. H., Li, P., Cadien, K. C., Brett, M. J., Luber, E. J., & Buriak, J. M. (2017). Understanding the effects of a high surface area nanostructured indium tin oxide electrode on organic solar cell performance [PMID: 29022714]. *ACS Applied Materials & Interfaces*, *9*(44), 38706–38715. https://doi.org/10.1021/acsami.7b10610

[93] Jayathilake, B. S., Chandrasekaran, S., Deutzmann, J. S., Kracke, F., Cornell, C., Worthington, M. A., Freyman, M. C., Jue, M. L., Spormann, A. M., Pang, S. H., & Baker, S. E. (2025). Additively manufactured high surface area 3d cathodes for efficient and productive electro-biomethanation. *ACS Electrochemistry*, *1*(4), 523–534. https://doi.org/10.1021/acselectrochem.4c00109

[94] NREL. (2021). Hybrid energy systems: Opportunities for coordinated research: U.S. Department of Energy (DOE), Energy Efficiency Renewable Energy (EERE). https://www.nrel.gov/docs/fy21osti/77503.pdf